Geochemistry, Geophysics, Geosystems®

AGU ADVANCING EARTH AND SPACE SCIENCE

RESEARCH ARTICLE
10.1029/2022GC010707

Key Points:

- The seasonal variations have an impact on the remanent magnetization in varved sediments

Correspondence to:
É. G. H. Philippe,
egh.philippe@gmail.com

Citation:
Philippe, É. G. H., St-Onge, G., Valet, J.-P., Godbout, P.-M., Egli, R., Francus, P., & Roy, M. (2023). Influence of seasonal post-depositional processes on the remanent magnetization in varved sediments from glacial Lake Ojibway (Canada). *Geochemistry, Geophysics, Geosystems*, *24*, e2022GC010707. https://doi.org/10.1029/2022GC010707

Received 14 SEP 2022
Accepted 10 FEB 2023

Influence of Seasonal Post-Depositional Processes on the Remanent Magnetization in Varved Sediments From Glacial Lake Ojibway (Canada)

Édouard G. H. Philippe[1,2], Guillaume St-Onge[2], Jean-Pierre Valet[1], Pierre-Marc Godbout[3,4], Ramon Egli[5], Pierre Francus[6], and Martin Roy[3]

[1]Sorbonne Paris-Cité, UMR 7154 CNRS, Institut de Physique du Globe de Paris, Paris, France, [2]Canada Research Chair in Marine Geology & GEOTOP, Institut des sciences de la mer de Rimouski (ISMER), Université du Québec à Rimouski, Rimouski, QC, Canada, [3]Département des sciences de la Terre et de l'atmosphère & GEOTOP, Université du Québec à Montréal, Montréal, QC, Canada, [4]Now at Geological Survey of Canada, Natural Resources Canada, Ottawa, ON, Canada, [5]Central Institute for Meteorology and Geodynamics, Vienna, Austria, [6]Centre Eau Terre Environnement (INRS-ETE), Canada Research Chair in Environmental Sedimentology & GEOTOP, Institut national de la recherche scientifique, Quebec, QC, Canada

Abstract The natural remanent magnetization (NRM) of high sedimentation rate sediments provides significant information about paleomagnetic secular variation of the Earth's magnetic field and can also potentially be used for stratigraphy. However, NRM acquisition depends on conditions inherent to the depositional environment. In addition to recording a precise annual chronology, varved sediments reflect marked annual sedimentary changes. The Earth's magnetic field does not vary significantly over such a short period, so magnetic changes recorded by varves are expected to reflect the influence of depositional parameters on the recording process. We focus here on a sequence of 27 ± 1 varves from the former proglacial Lake Ojibway (~8.5 ka cal BP) from which individual cm-thick summer and winter beds were sampled. Paleomagnetic, granulometric and geochemical analyses were conducted on each bed. A mean inclination shallowing of 24.3° is observed in winter beds, along with an 11.3° shallowing in summer beds. Magnetic declinations follow, on average, the expected field direction, but differences of up to 20° occur between successive beds. Summer beds are thicker than winter beds and have stronger magnetic susceptibility, higher Ca/Fe ratios and coarser sedimentary and magnetic grains. This grain size pattern reflects the input of coarser detrital particles during summer, while the finer fraction remained in suspension until it was deposited in winter. A combination of differential compaction between the winter and summer beds, seasonally varying physical and magnetic properties of sediments, and delayed NRM acquisition explains the variable and coercivity-dependent inclination shallowing.

1. Introduction

Acquisition of detrital remanent magnetization (DRM) by sediments is a complex phenomenon that results from a statistical alignment of magnetic grains by the local geomagnetic field (DRM $\approx \xi B$, where ξ is the sediment response function and B the geomagnetic field). The sediment response function depends on several parameters related to the depositional environment, sediment matrix, and nature of magnetic grains. Numerous experiments and models aimed at simulating depositional processes and sediment magnetization have been proposed over the last 60 years (Nagata, 1961; Philippe et al., 2022; Spassov & Valet, 2012; Tanty et al., 2016; Tauxe, 1993; Tauxe et al., 2006; Yoshida & Katsura, 1985). However, a major limitation of laboratory deposition experiments is the impossibility to simulate natural sedimentation conditions in the absence of adequate scaling that accounts for the much longer duration of the magnetization process in nature (Katari et al., 2000; Spassov & Valet, 2012; Tauxe, 1993; Tauxe et al., 2006; Valet et al., 2017; Yoshida & Katsura, 1985). Experiments are also constrained by the limited size of containers used for deposition, which imposes a high concentration of suspended sediment, and the lack of adequate simulation of the hydrodynamic environment (Spassov & Valet, 2012; Valet et al., 2017; Yoshida & Katsura, 1985). Despite these limitations, it is possible to constrain the role of specific parameters in magnetic particle alignment using artificial laboratory-deposited mixtures (Valet et al., 2017). It is also possible to compare the results of laboratory experiments with natural analogs of rapidly deposited sediments. The role of lithology and grain size in the magnetization process can be studied in turbidite sequences that provide useful indications about the influence of hydrodynamic conditions and the role played by magnetic and sediment

grain sizes (Philippe et al., 2022; Tanty et al., 2016). Another interesting approach focuses on varved sediments (Mellström et al., 2015; Nilsson et al., 2018), which can potentially provide highly detailed magnetic records with annual temporal resolution.

Here, we investigate the magnetic properties of a 61-cm-long sediment sequence composed of 27 ± 1 annual varves from former proglacial Lake Ojibway (Godbout et al., 2019). Within this sequence, we conducted additional analyses on a 7-year packet of varves, where the role of secular variation in the record variability cannot exceed a few degrees, in order to investigate the causes of seasonal differences.

2. Origin of Samples and Geological Context

Lake Ojibway formed during the last deglaciation by accumulation of meltwater that was trapped between the decaying ice margin of the Laurentide Ice Sheet (LIS) to the north and elevated land of the Hudson Bay/St. Lawrence River drainage divides to the south, where meltwater overflow is routed through the Ottawa River Valley (Figure 1a). This ice-dammed lake occupied vast portions of NE Ontario and NW Quebec (Canada) following northward ice retreat and reached its greatest extent ~8.5 ka cal BP, when it presumably merged with Lake Agassiz to the west to form a larger meltwater reservoir (e.g., Dyke, 2004; Thorleifson et al., 1996). Lake Ojibway disappeared at around 8.2 ka cal BP (e.g., Brouard et al., 2021; Roy et al., 2011), following its drainage through the Hudson Bay ice dam (e.g., Clarke et al., 2004; Lajeunesse & St-Onge, 2008).

The high melt rate of the LIS southern margin led to varve deposition in the Ojibway Basin, which formed an important sedimentary archive that documents early Holocene regional deglacial ice dynamics and lake paleohydrology (e.g., Antevs, 1925; Breckenridge et al., 2012). In general, glaciolacustrine varves are characterized by alternating couplets of light- and dark-colored layers of silt/clay-sized sediments that reflect seasonal sediment input variations. During summer, pronounced melting releases large amounts of coarse-grained detrital material to the basin with concomitantly high deposition rates, while cold wintertime temperatures considerably reduced meltwater and sediment inflow, with attendant lake ice cover favoring settling of suspended fine-grained sediment (Smith & Ashley, 1985).

A 3.6 m-long sediment sequence containing 231 ± 7 varves that crops out on the shore of Lake Matagami, Quebec (49°56′43.494″N, 77°13′4.663″W), was studied here (Figure 1b) (Godbout et al., 2019). Paleogeographic considerations indicate that the sequence was deposited in ~150 m water depth (Godbout et al., 2020; Veillette, 1994). This section was sampled twice using 61-cm-long oriented metal gutters (bottom-G7 to top-G1) with ends that stratigraphically overlap each other. The gutter orientation was used to calculate the true declination. Each gutter was duplicated to obtain one sequence for sedimentary studies and one for magnetic measurements. A small gap of a few millimeters is possible between the sediment and magnetic gutter. We report here measurements from the bottom of G7 gutter (27 ± 1 varves), which contains the oldest sediments of the sequence. This interval also contains the thickest varves with a 2.01 cm a^{-1} average sedimentation rate.

3. Methods

3.1. Sedimentary Analyses

Non-destructive measurements were performed at INRS-ETE, Québec City. High-resolution tomograms (1 pixel = 100 × 100 μm) of the varves were obtained with a Siemens SOMATOM Definition AS+ 128 CT-Scanner (Boespflug et al., 1995; Crémer et al., 2002; Fortin et al., 2013; St-Onge et al., 2007). The resulting images are displayed in gray scale, with darker and lighter zones representing lower and higher sediment densities, respectively.

X-ray fluorescence and optical scans were obtained using an ITRAX core scanner from Cox Analytical Systems. Analyses were performed using a 500 μm resolution and 10 s counting time (Croudace et al., 2006; Francus et al., 2002; Rothwell et al., 2006; St-Onge et al., 2007) to provide downcore geochemical profiles of a wide range of elements. Grain-size analyses were also carried out for each sediment layer, that is, the center of the summer and winter beds contained within the G7 gutter. Sediment particle size was measured at UQAM using a Microtrac Bluewave/S3500-SDC laser diffraction particle size analyzer. Finally, organic matter contents were determined by loss-on-ignition using a protocol adjusted for the clay content and composition of the carbonate-rich Ojibway sediments (i.e., 48 hr oven-dried at 60°C and heated for 4 hr at 450°C; Godbout et al., 2019). A thin section was also sampled in the G7 gutter, following the method of Francus and Asikainen (2001).

10.1029/2022GC010707

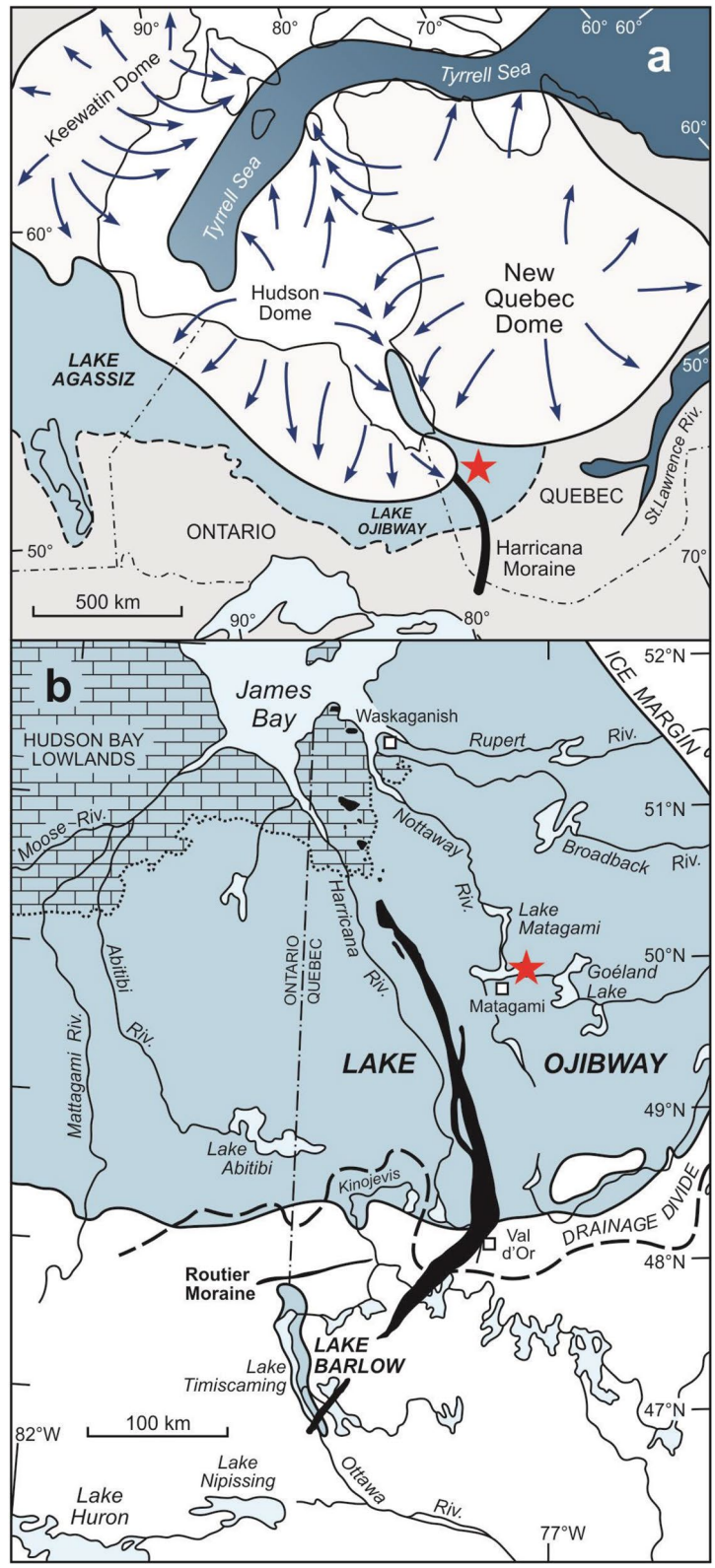

Figure 1. Locations of (a) Lake Ojibway (b) and the modern remnant, Lake Matagami, during deglaciation ~8500 cal BP. Stars indicate the site location. Blue arrows are glacial flow-lines associated with residual ice domes. Modified from Roy et al. (2015).

3.2. Magnetic Measurements

Magnetic measurements were performed using 2 × 2 cm square section U-channels. U-channel measurements average remanent magnetization variations over 7-cm (Philippe et al., 2018) and therefore smooth details of stratigraphic features inherent to the finely laminated sequence. For individual varve analysis, 1 cm^3 plastic cubes were used to sample a fine sediment slice from each stratigraphic level. All the remanent magnetization measurements of these samples were made with a special 3D printed sample holder. The resolution obtained using this technique remained evidently too low to resolve millimetric varves, but it was adequate for individual thicker varves.

The natural remanent magnetization (NRM) was measured using a 2-G Enterprises Model 755-1.65 cryogenic magnetometer with direct current (DC) SQUID sensors at the Institut de Physique du Globe de Paris (IPGP). The NRM of all samples was demagnetized along three orthogonal axes using alternating fields (AF) up to 140 mT in 10 mT steps. Anhysteretic remanent magnetization (ARM) was then imparted in the presence of a 0.5 mT DC field and a 60 mT maximum AF field. Additional magnetic measurements were performed to characterize the magnetic mineralogy, magnetic grain size and magnetic anisotropy across winter and summer beds. The S-ratio defined as $S = ½ (1 - IRM_{-0.3T}/SIRM_{1T})$ (Bloemendal et al., 1992) represents the ratio between low and high coercivity minerals and was calculated after remagnetizing the samples in a 1 T field (SIRM) and subsequently in a 0.3 T (IRM) reversed field. Measurements of magnetic susceptibility during heating to 600°C were performed using a KLY3 Kappabridge system. The anisotropy of the magnetic susceptibility was measured using the KLY3 Kappabridge system to check sedimentary fabrics. Hysteresis loops were obtained using a PMC Series 3900 vibrating sample magnetometer (VSM).

Detailed rock magnetic analyses of two samples representative for winter (G7 35.5 cm) and summer (G7 39.6 cm) beds were derived from high-resolution first-order reversal curve (FORC) measurements performed with a Lake Shore 8600 Series VSM at the ZAMG material magnetism laboratory in Vienna. For each sample, 950 curves were acquired in steps of $\Delta B = 0.25$ mT. Nine collections of identical curves have been stacked to increase the signal-to-noise ratio and capture a minor contribution from non-interacting single-domain (SD) particles. FORC measurements have been processed with VARIFORC (Egli, 2013) and the following parameters: minimum smoothing factor $s = 6$, the rate of smoothing factor increase $\lambda = 0.2$, smoothing factor limitation across the central ridge: $s_b = 3$. Coercivity distributions associated with the FORC measurements (Egli, 2021) have been extracted with VARIFORC.

Additional information on the NRM carriers and the nature of the small (<3.8°) dependence of the NRM direction on the AF demagnetization has been obtained by fitting the NRM data of representative winter and summer beds with two vector components, such that the NRM magnetization M_{nrm} remaining after the application of a demagnetizing field B_{af} is given by

$$\mathbf{M}_{\mathrm{nrm}}(B_{\mathrm{af}}) = \sum_{i=1}^{2} a_i \mathbf{n}_i \left[1 - F(B_{\mathrm{af}}, \mathbf{p}_i)\right] \quad (1)$$

where F is the integral of a probability density function f whose shape is controlled by the vector of parameters $\mathbf{p}_i$, a_i is the total NRM contribution of the ith component, and $\mathbf{n}_i$, the unit vector representing the direction of this component in a coordinate system where x points to the North, y to the West, and z upwards. In analogy with coercivity analysis, f is interpreted as the coercivity distribution of magnetic minerals that recorded the same paleomagnetic direction, and $1 - F(B_{af})$ as a function describing the fraction of the original magnetization carried by these minerals after a demagnetizing step with B_{af}. The Burr Type XII distribution has been chosen as a model for f (Zhao et al., 2016), due to its resemblance to the generalized Gaussian function commonly used for the coercivity analysis of AF demagnetization curves (Egli, 2004), and the fact that F can be expressed analytically. Least-squares regression of NRM data with Equation 1 is based on the minimization of mean square vector residuals given by

$$r^2 = \sum_{i=1}^{2} \left\| a_i \mathbf{n}_i \left[1 - F(B_{\mathrm{af}}, \mathbf{p}_i)\right] - \mathbf{M}_{\mathrm{nrm}}(B_{\mathrm{af}}) \right\|^2 \quad (2)$$

Like classic parametric coercivity analysis (Egli, 2003), least-squares regression yields multiple solutions, depending on the initial parameter choice. The multiplicity of solutions has been explored using 1,000 regression results from randomly chosen initial parameter vectors $\mathbf{p}_i$, direction vectors $\mathbf{n}_i$, and NRM contributions a_i, using

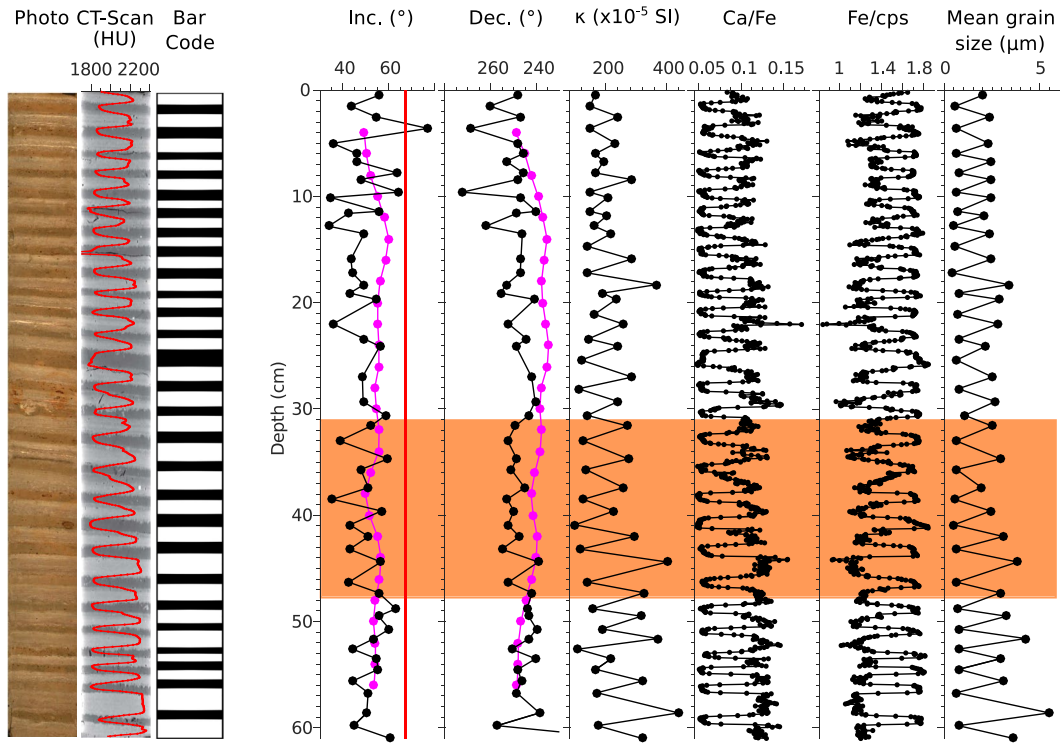

Figure 2. From left to right as a function of depth within the G7 gutter core: core photograph, HU numbers related to sediment density derived from the CT-Scan images and composite column that summarizes the succession of winter (black) and summer (white) beds. Downcore magnetic (inclination, declination, magnetic susceptibility) and sediment (Ca/Fe ratio, Fe/cps and grain size) parameters. The inclination and declination indicated in black correspond to single sample measurements and are compared with U-channel measurements (pink). The red line corresponds to the geocentric axial dipole value. The Fe profile in the peak area is normalized by the counts per second (cps) at the corresponding depth. Orange shading represents the studied interval illustrated in Figure 7.

the built-in FindMinimum function in Wolfram Mathematica. Results have been found to converge to a limited number of discrete solutions (typically ~10). Only the 1–4 solutions with the smallest r^2 and smallest maximum angular residuals were considered for further analysis.

4. Results

4.1. Lithological and Chemical Characteristics

A photograph of the G7 series along with CT-scan profiles of sediment density variations between higher density summer (light) and lower density winter (dark) beds (e.g., Boespflug et al., 1995; St-Onge et al., 2007) are shown in Figure 2. Grain size variations within the G7 interval are also shown as a function of depth, revealing systematic differences between silty summer (2.8 ± 0.8 µm mean grain size) and clayey winter beds (0.7 ± 0.1 µm mean grain size) (ISO 14688-1:2002). Grain size and XRF data reveal that summer silty beds are richer in Ca and winter clayey beds in Fe (Figure 2), confirming the observations of Stroup et al. (2013) on Ojibway varves. Along with similar studies on varved sediments (Croudace et al., 2006; Rothwell et al., 2006; Striberger et al., 2011; Stroup et al., 2013), we used the median Ca/Fe value to delimit the positions of the summer bed maxima and winter minima with ±500 µm accuracy to produce the bar code of the winter/summer beds shown in Figure 2. Downcore magnetic susceptibility (κ) changes at room temperature largely exceed the typical values of paramagnetic minerals (Moskowitz, 1991), therefore depicting mainly downcore changes in iron oxide concentration and/or mineralogy.

A thin section of two successive varves under normal (Figure 3a) and polarized light (Figure 3b) highlights the sedimentological and lithological differences between the summer and winter beds. Each summer bed contains load casts at the bottom, micro-laminations in the mid-part and coarser particles, calcite aggregates and minute traces of bioturbation in the upper part, while winter beds appear homogeneous and massive.

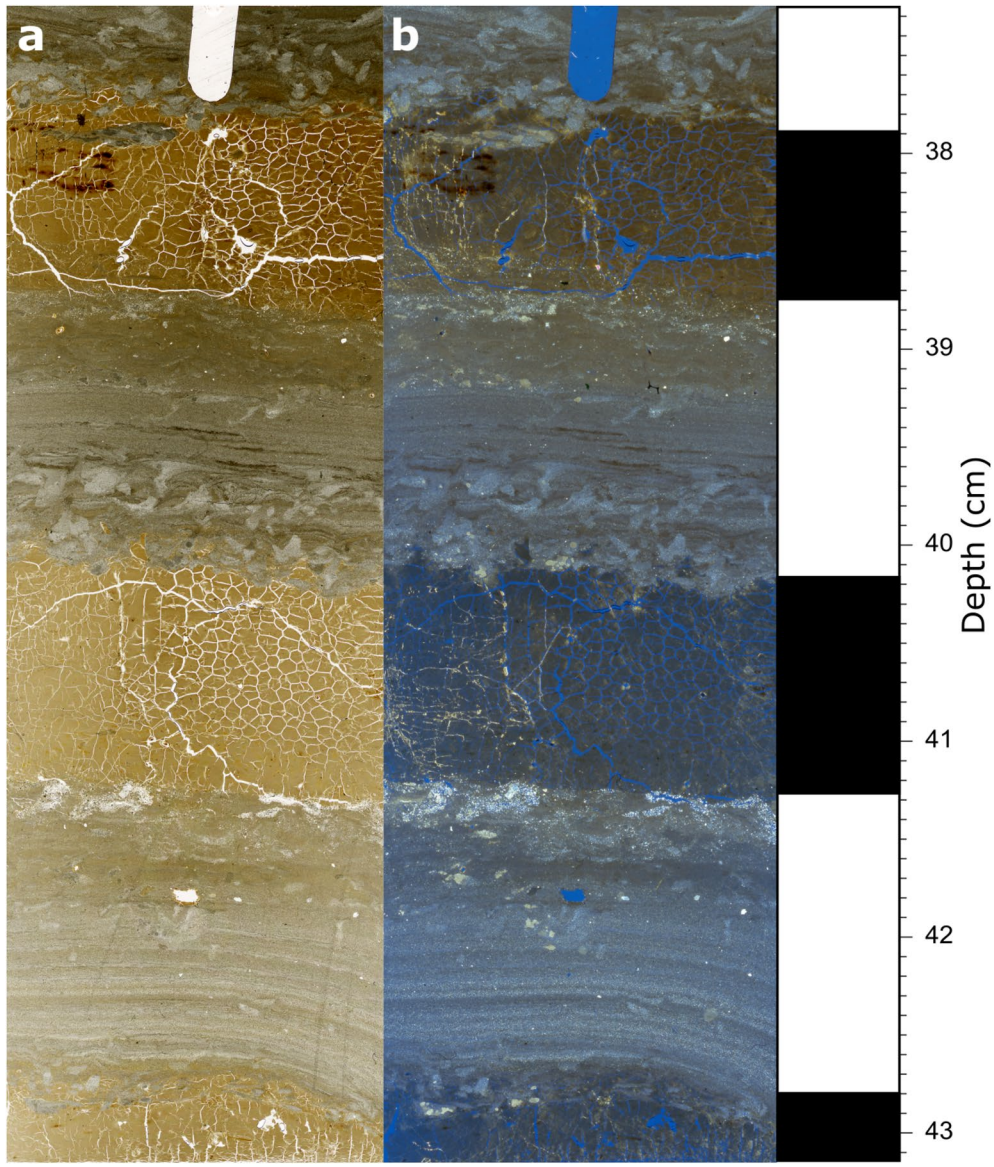

Figure 3. Photograph of a thin section from core G7 under (a) normal light and (b) polarized light. A bar code is shown on the right with white and black zones, corresponding respectively to summer and winter beds. The polygonal network of cracks was produced during thin-section production in the clay-rich sediment.

4.2. Bulk Magnetic Properties

Thermomagnetic curves for summer and winter beds are similar (Figure 4). In both cases, a rapid magnetization decrease was observed between 560°C and 610°C. This decrease is consistent with the Curie temperature of magnetite (580°C), with no indication of higher Curie temperatures. Thermally stable magnetite is therefore the main magnetization carrier in summer and winter beds. A minor decrease in κ occurs between the peak at ~280°C and the onset of the Curie transition in summer beds. This decrease is irreversible, as seen from the cooling curves, and indicates a progressive transformation of a ferrimagnetic phase to a less magnetic or a nonmagnetic one above 280°C. This behavior is compatible with the presence of greigite (Dekkers et al., 2000; Roberts et al., 2011), as also hinted by the FORC diagrams (see below). The same signature, albeit less pronounced, is also present in the heating curves of the winter beds. The S-ratio values range from 99.3% to 100%, confirming the absence of high-coercivity minerals like goethite or hematite.

Representative high-quality NRM demagnetization diagrams (Cogné, 2003) are shown in Figure 5 for the same summer and winter bed samples of Figure 4. All samples are progressively demagnetized up to the maximum AF

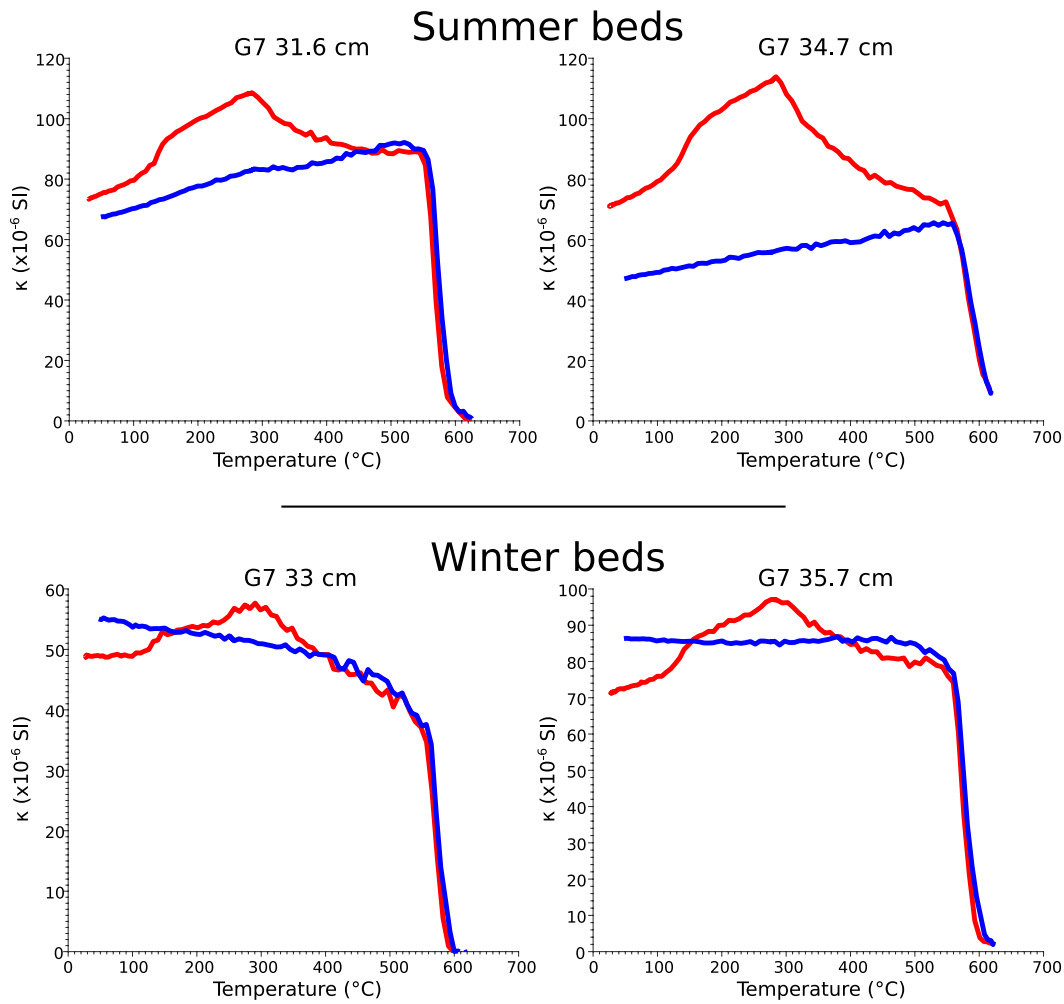

Figure 4. Thermomagnetic curves of low-field susceptibility versus temperature for two summer and two winter beds. Heating (cooling) curves are shown in red (blue).

field of 140 mT, with no evidence of overprints or viscous behavior. The AF field required to demagnetize the sediments is unusually large, and likely reflects the presence of very elongated magnetite grains. The characteristic directions are defined unambiguously by slightly curved lines that pass through the origin, with maximum angular deviation (MAD) values generally lower than 1°. The characteristic remanent magnetization declination and inclination records are plotted in Figure 2 for comparison with other parameters. Also, shown in pink (Figure 2) are the directions derived from low-resolution U-channel measurements. As expected, the response curve of the magnetometer has considerably smoothed yearly variations that are resolved with discrete sample measurements (Philippe et al., 2018).

Declinations of discrete samples oscillate between 240° and 265°, sometimes between consecutive layers, but do not display a clear long-term trend. The amplitude of yearly variations can reach 30° within the upper 15 cm of the sequence, while it does not exceed 10° below this depth. About 5°–10° declination differences can result from uncertainties such as those generated by sampling of tiny specimens and/or reflect lithological and/or sediment matrix influences on magnetic particle alignment. The declination was used to establish the chronostratigraphy of laminated glaciolacustrine sediments (Ridge et al., 1990); therefore, averages over few summer and winter beds are expected to yield reliable paleofield directions.

Seasonal inclination variations reach 40° in the upper part of the record and decrease in amplitude below 12–15 cm. Inclinations are significantly shallower than the 67.2° value predicted by the geocentric axial dipole (GAD) at this latitude. Given the short time interval (~25 years) covered by the G7 record, these variations are unlikely to reflect significant geomagnetic changes, although local non-dipole (ND) fields can generate some

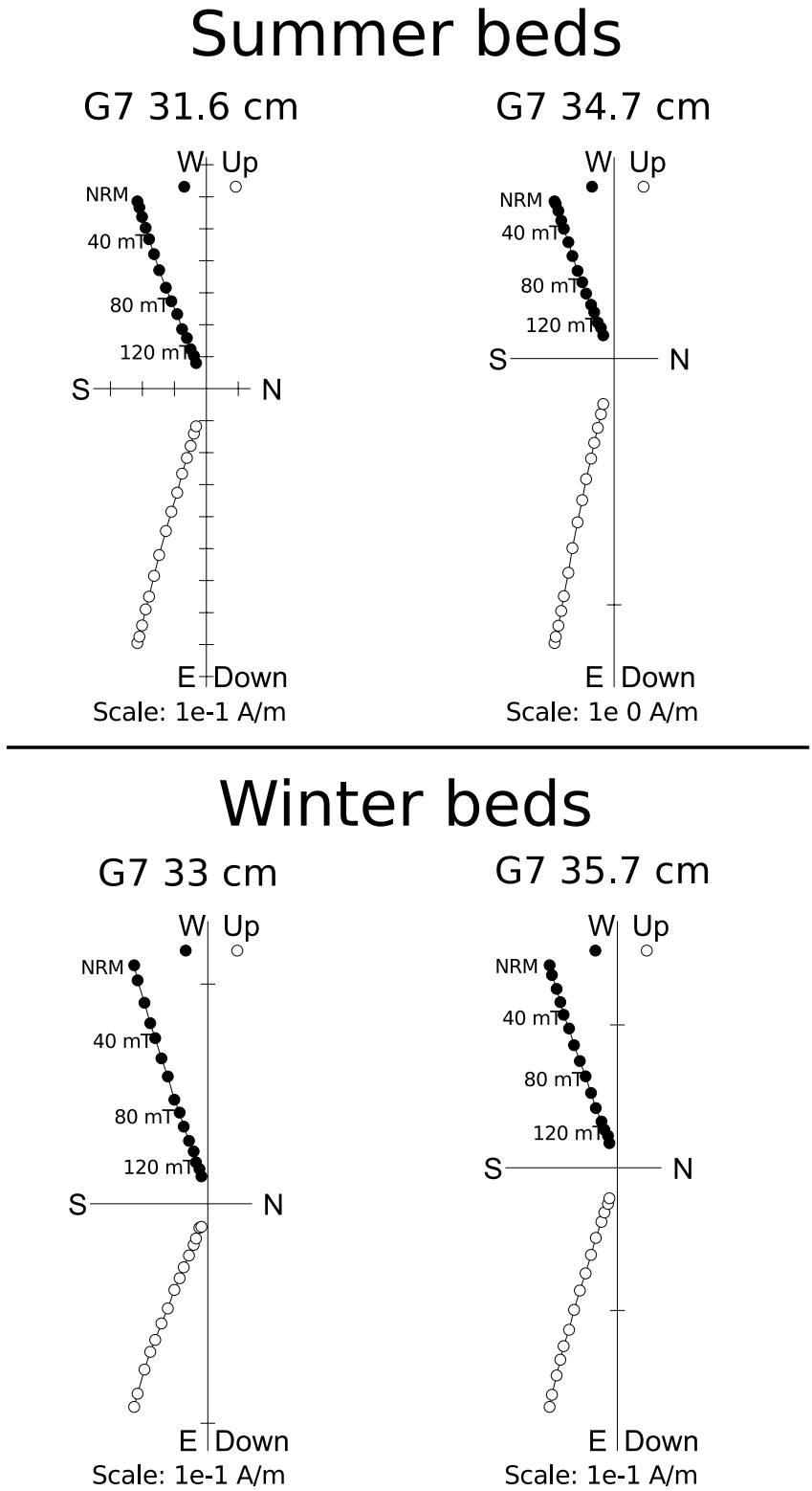

Figure 5. Demagnetization diagrams. Vector end-point diagrams for two summer and two winter beds. Solid symbols correspond to projections onto the horizontal plane, while open symbols represent projections onto the vertical plane.

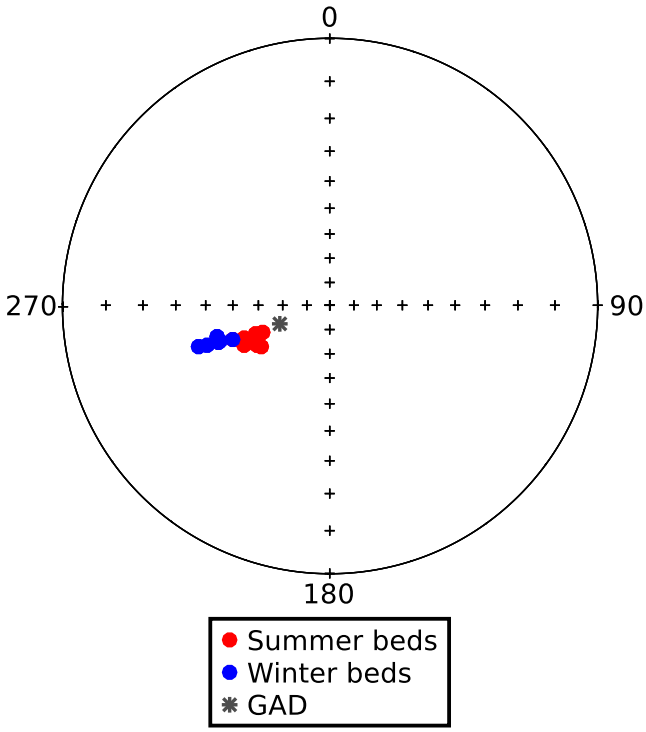

Figure 6. Stereoplot (equal angle) of magnetic directions recorded by the beds within the studied interval of core G7. Red and blue dots indicate summer and winter beds, respectively. The gray asterisk indicates the geocentric axial dipole (GAD) direction at the site. The summer bed inclinations are closer to the GAD value at the site than the winter ones.

deviations from the GAD inclination. The ND present-day value explains deviations of ~0.075°a^{-1} (Thébault et al., 2015). ND components can represent up to 20% of the dipole field, yielding GAD deviations of up to 15°. During periods of low dipole intensity, these deviations are further amplified. Global paleointensity compilations (Barletta et al., 2010) indicate that 8.5 ka cal BP ago (the age of these sediments), the dipole was about 10% weaker than at present, which is insufficient to account for inclinations that are 30° lower than the GAD value. Therefore, other factors must be considered to explain the observed inclination shallowing.

Given the millimetric size of individual beds in the upper part of the sequence, we focused on the interval with the thickest layers between 48 and 31 cm, which comprises 7 summer beds and 6 winter beds (highlighted in orange in Figure 2) and analyzed each bed separately. Successive inclination and declination values are plotted in stereographic projection (Figure 6) and against depth (Figure 7). These data reveal that the summer and winter beds have similar declinations, but they also confirm that winter inclinations (41.7° ± 4.3°) are 13° shallower than the summer ones (54.7° ± 3.3°). All values remained lower than the GAD inclination of 67.2° (Figure 7). Stacked geomagnetic field records at the same latitude (~50°N) and the same period (~8500–9000 cal BP) are characterized by steeper inclinations, that is, 66.1° ± 4.1° for the eastern Canadian stack and 65.4° ± 1.9° for the west Eifel stack from Germany. The mean of these two stacks over this period, which is 66° ± 4°, is similar to the GAD inclination at the site latitude. From this, we deduce an average inclination shallowing of 11.3° ± 7.3° for summer beds and 24.3° ± 8.3° for winter beds relative to the geomagnetic field at the same latitude and over the same time interval. No significant geomagnetic field intensity variations have occurred during such a short period, so NRM/ARM values (Figure 7) provide information about seasonal changes in the NRM acquisition efficiency ξ. The NRM acquisition efficiency can be affected by the depositional environment (e.g., turbulence), by the nature of detrital material (in particular, its tendency to flocculate), and by the nature of the magnetic minerals (e.g., their magnetic moment), and by post-depositional processes (e.g., compaction).

The ratio between the ARM and the low-field-volume susceptibility (κ) is a proxy for the grain size of remanence carriers, with high values being characteristic for SD minerals (Figure 7). In the absence of strong paramagnetic contributions, as it is the case for core G7, ARM/κ has the advantage of being primarily sensitive to the size of ferrimagnetic minerals, thus avoiding biases related to variable concentrations of hematite, goethite, and other high-coercivity minerals (Stoner & St-Onge, 2007). As far as the differences between summer and winter beds are concerned, ARM/κ is negatively correlated with NRM/ARM, with higher values pointing to smaller magnetic grains occurring systematically in winter beds. The day plot (Day et al., 1977; Dunlop, 2002) also shows systematic differences between summer and winter beds, which fall into two separate clusters (Figure 8). While both clusters are contained in the so-called pseudo-single-domain (PSD) range of M_{rs}/M_s and B_{cr}/B_c, the winter cluster is significantly shifted toward larger values of B_{cr}/B_c, away from the grain size trend or SD-multidomain mixing trend typical of magnetite particles. This shift is typical for samples containing large number of superparamagnetic (SP) particles (Dunlop, 2002).

4.3. Magnetic Mineral Components

High-resolution FORC measurements of two representative samples provide further details about the nature of NRM carriers in the winter and summer beds (Figure 9). Both are characterized by FORC diagrams that can be explained by the superposition of typical signatures from two magnetic domain classes: (a) SD particles, and (b) PSD particles, which are too large to contain a single domain and too small to accommodate several well-defined magnetic domains (Nagy et al., 2019). The SD component is characterized by a narrow horizontal ridge (central ridge) centered near $B_u = 0$ (Egli et al., 2010), which contributes to ~10% of the total FORC magnetization in the winter bed, and ~2% in the summer bed (Figures 9c and 9d). The associated SD coercivity

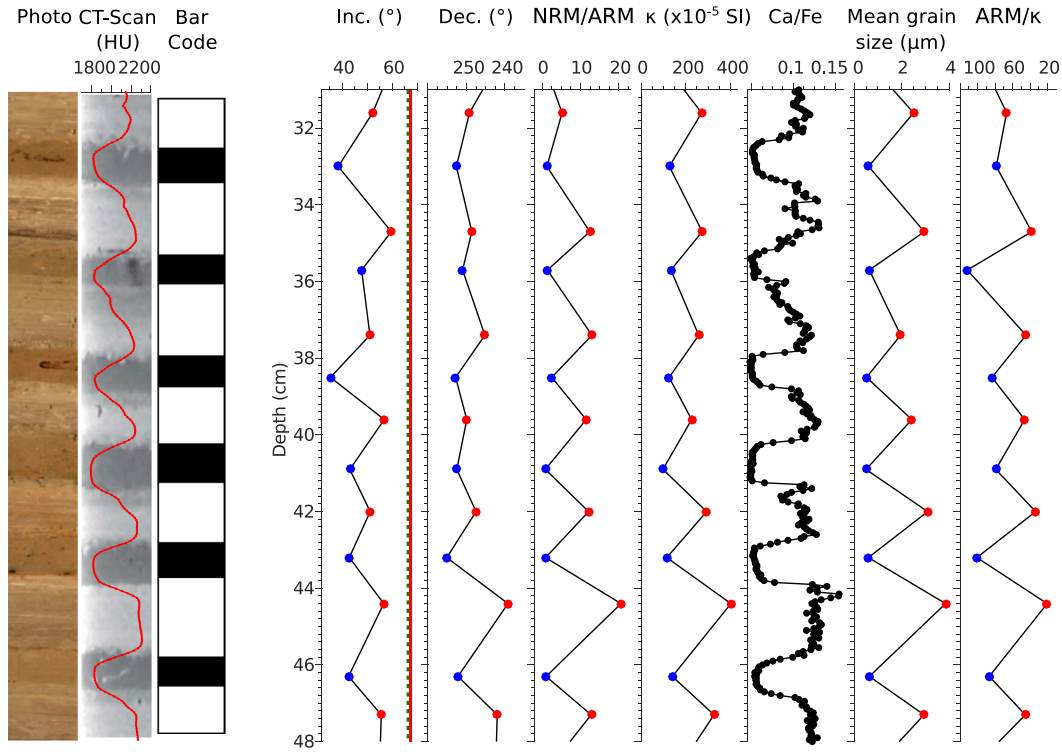

Figure 7. Magnetic and sediment properties for each bed from the 7-year interval are outlined in orange in Figure 2. Red and blue data points correspond to summer and winter beds, respectively. The red line and green dashed lines on the inclination plot represent, respectively, the geocentric axial dipole and inclination values at the same latitude around 8500–9000 cal BP.

distributions, which extend up to ~100 mT, are typical of non-interacting magnetite particles but have markedly different shapes. In summer beds, the nearly zero amplitude at $B_c = 0$ and the peak at $B_c \approx 25$ mT are compatible with low-coercivity magnetofossils, that is, chains or chain fragments, made of equidimensional crystals (Amor et al., 2022; Egli, 2004). In winter beds, the peak at $B_c = 0$ and the rapid decrease in the 0–50 mT range are typical of magnetite particles lacking a strong intrinsic anisotropy source, and with a size distribution across the lower limit of the SD stability range (Egli, 2021; Lanci & Kent, 2018). This means that a significant fraction of the SD particles in winter beds are SP, as confirmed by the B_{cr}/B_c shift in the Day plot (Figure 8). The central ridge in the FORC diagram of the winter bed is similar to that of pedogenic magnetite in soils (Egli, 2021), but its characteristics are also compatible with authigenic magnetite, as far as individual magnetic particles are well dispersed in the sediment matrix. Unfortunately, a term of comparison for the FORC signature of authigenic magnetite does not exist, as synthetic examples, such as magnetite produced by dissimilatory iron-reducing bacteria (Moskowitz et al., 1993), or by the reduction of precursor minerals (Till et al., 2017), contain clusters of strongly interacting particles incompatible with the central ridge signature of Figure 8d.

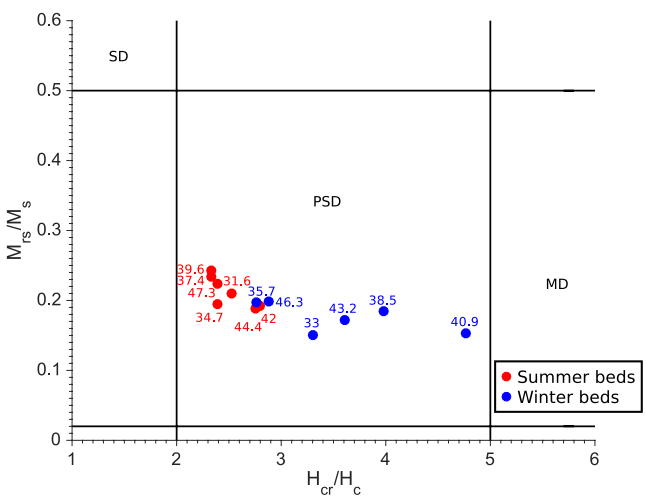

Figure 8. Day plot for beds within the 7-year interval. Red (blue) data points are for summer (winter) beds.

The PSD contribution of winter and summer beds is characterized by triangular contour lines in the upper half of the FORC diagram, which diverge toward $B_c = 0$, and a more complex signature in the lower half, with a characteristic indentation of contour lines caused by the superposition of negative contributions along $B_c = 0$ and along the descending diagonal $B_c = -B_u$ (Egli, 2021; Roberts et al., 2017). These characteristics are typical of a broad distribution of grain sizes ranging from the upper SD threshold to small multidomain particles. The associated coercivity distribution is broad, with a median of ~80 mT and a range extending to >200 mT. The coercivity range is unusually large value for magnetite with comparable FORC signatures (e.g., Lascu

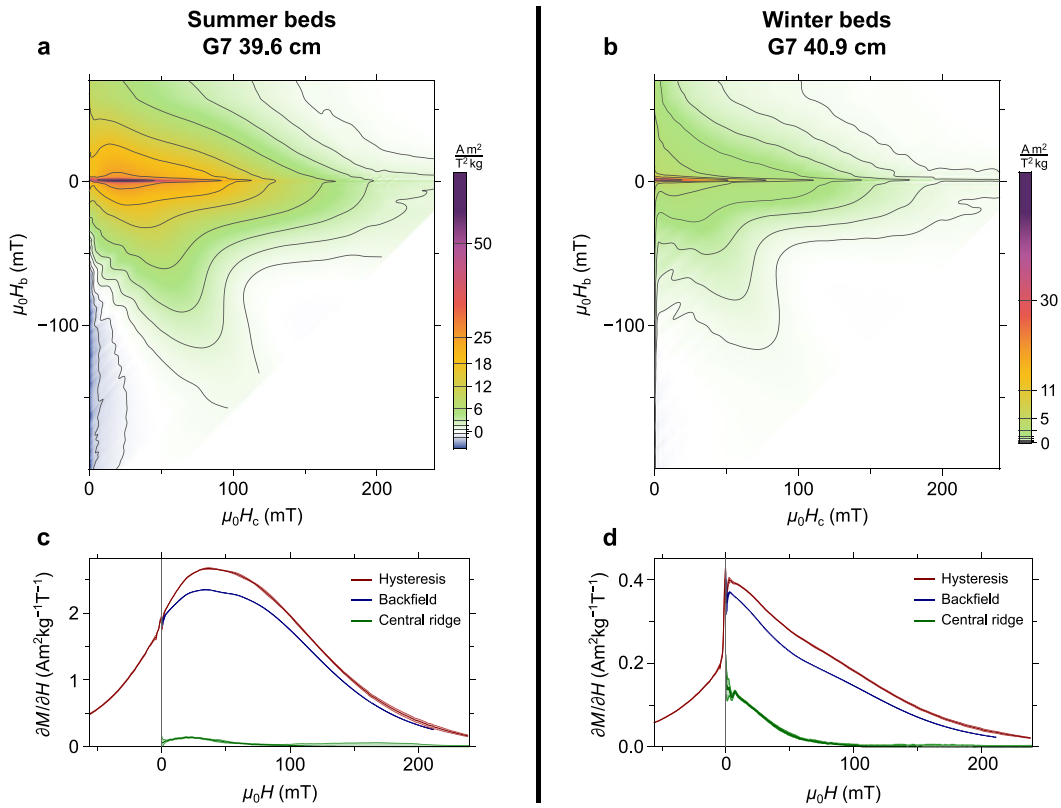

Figure 9. High-resolution first-order reversal curve (FORC) diagrams for the summer bed at 39.6 cm (a) and the winter bed at 40.9 cm (b). (c, d) Backfield, hysteresis, and central ridge coercivity distributions derived from the original FORC measurements of the summer and winter beds, respectively. All diagrams and coercivity distributions were generated using VARIFORC built-in functions (Egli, 2013).

et al., 2018) and likely associated with exsolved magnetite inclusions in silicate, whose median destructive fields can reach up to ~90 mT (Feinberg et al., 2005).

The coercivity distributions derived from hysteresis and backfield demagnetization data contained in the FORC measurements (Figures 9c and 9d) feature a main peak at ~40 mT (summer bed) and ~0 mT (winter bed), as well as a secondary peak, or shoulder, around 70–80 mT, which is associated with the common PSD signature of summer and winter beds. The main peak at ~0 mT of the winter bed reproduces the coercivity distribution of the central ridge, with a ~1:3 ratio between the central ridge and backfield coercivity distribution amplitude that is similar to that of pedogenic magnetite (Egli, 2021). The main peak at ~40 mT of the summer bed, on the other hand, is much larger than the central ridge distribution and can be explained by FORC contributions characterized by nearly oval contour lines around the central ridge. The B_c range of these contours, comprised between ~20 and 100 mT, and their limited vertical extension are compatible with the typical signature of authigenic greigite (Egli et al., 2010; Roberts et al., 2011). The coexistence of greigite FORC signatures with a weak central ridge (Rowan & Roberts, 2006) might be explained by the coexistence of magnetite and/or greigite magnetofossils (A. P. Chen et al., 2014) with diagenetic greigite during the early stages of greigite diagenesis. As discussed above, the presence of minor greigite contributions in summer beds is also supported by $\kappa(T)$ measurements.

Overall, summer and winter beds appear to contain a mixture of PSD magnetite grains, likely of detrital origin, and distinct populations of SD particles, including a minor greigite contribution in the summer beds, and dispersed magnetite particles of secondary origin in the winter beds. The S-ratio (Bloemendal et al., 1992) does not significantly differ between summer and winter beds (Figure 4), as expected from the absence of high-coercivity minerals such as pyrrhotite and hematite.

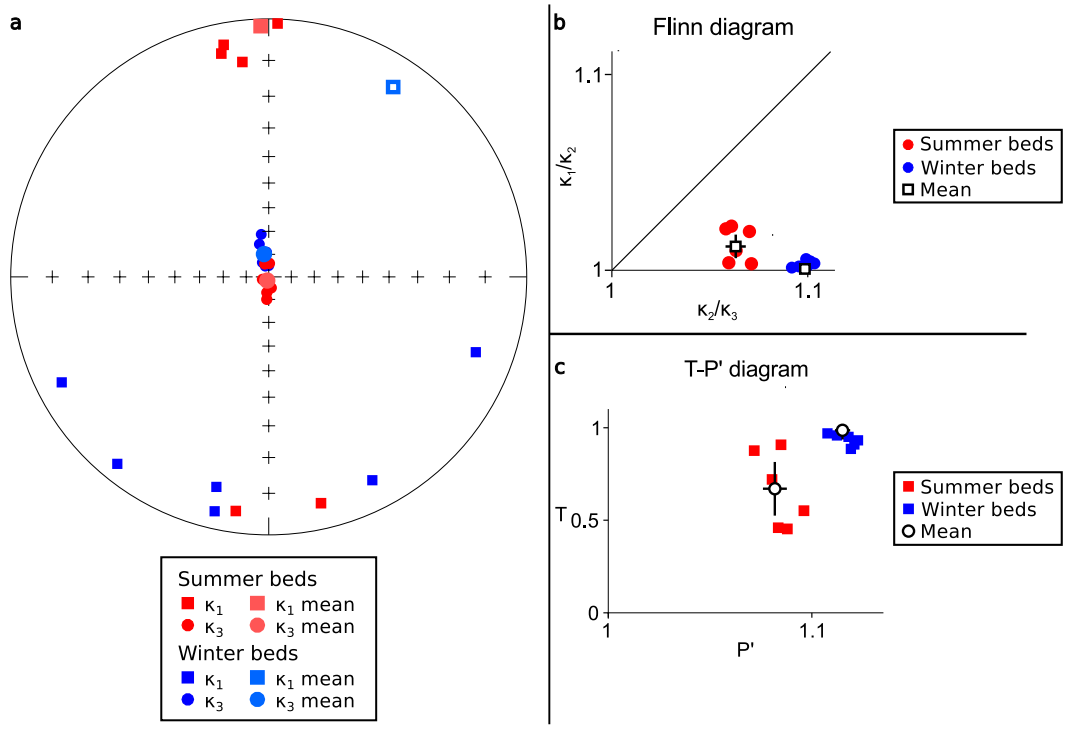

Figure 10. (a) Stereographic (equal angle) projection of the κ_1 and κ_3 axes of the magnetic susceptibility ellipsoid. (b) Flinn diagram, where κ_1/κ_2 represents the lineation and κ_2/κ_3 the foliation. (c) T–P' diagram of the shape factor $T = (2\log \kappa_2 - \log \kappa_1 - \log \kappa_3)/(\log \kappa_1 - \log \kappa_3)$ as a function of the corrected degree of anisotropy $P' = \exp(\sqrt{2\Sigma_i(\eta_i - \eta)^2}$ with $\eta_i = ln(\kappa_i)_{i=1,2,3}$ and $\eta = (\eta_1 + \eta_2 + \eta_3)/3$ (Jelinek, 1981). Red and blue dots indicate summer and winter beds, respectively.

4.4. Magnetic Fabric

Directions of the principal axes of the magnetic susceptibility tensor are shown in Figure 10a, with κ_1 corresponding to κ_{max} and κ_3 to κ_{min}. As expected for normal sedimentary fabrics, κ_{min} points vertically, especially in summer beds, meaning that the long axis of non-SD magnetic particles tends to lie horizontally. The axes of κ_{max} are sub horizontal and oriented N-S in the case of summer beds, while a wide horizontal scatter is observed for the winter beds. The Flinn diagram in Figure 10b shows the shape of the magnetic susceptibility tensor in terms of (κ_1/κ_2) versus foliation (κ_2/κ_3) (Cogné, 2003; Jelinek, 1981). The shape factor (Figure 10c) provides information on the ellipsoid oblateness ($T > 0.5$) as a function of the corrected degree of anisotropy P' (Jelinek, 1981), which measures the deviation from the spherical shape. Both winter and summer beds have oblate anisotropy, with almost perfectly oblate summer beds and slightly more anisotropic winter beds.

Differences between the magnetic fabric of summer and winter beds might originate from physical processes, such as the effect of bottom currents on magnetic grain deposition and compaction, or from differences in the type of magnetic carriers. Winter beds contain a significant amount of SD magnetite: the superposition of the inverse fabric of SD particles with the normal fabric of larger detrital particles might explain the scatter of κ_{max} and the deviation of κ_{min} from the vertical. The preferential N-S alignment of κ_{max} in summer beds, on the other hand, might be due to the alignment of magnetic grains by bottom currents during deposition. Finally, the lower NRM inclination of winter beds might be explained by the stronger magnetic fabric (as seen on P') associated with higher clay content (Borradaile & Almqvist, 2008), and, possibly, a stronger degree of compaction.

4.5. Origin of Curved Zijderveld Plots

All samples, regardless of their provenance from summer or winter beds, show a slight change in magnetization direction as NRM is progressively removed. The absence of a sharp transition between two linear regimes in the examples of Figure 5 suggests that the NRM is characterized by two paleomagnetic endmembers with completely overlapping coercivity ranges. The parameterization of the coercivity distribution of the two endmembers with

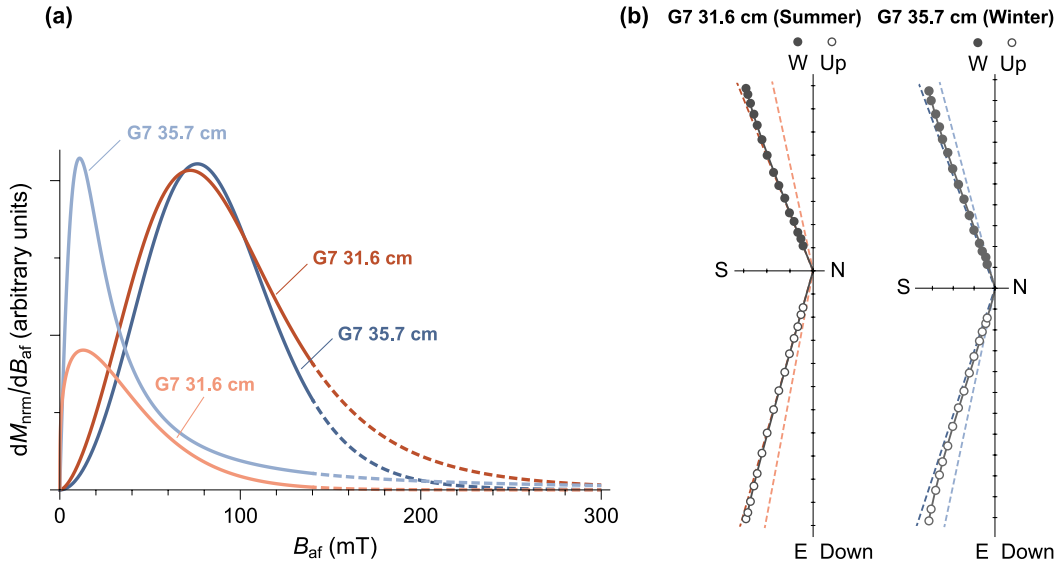

Figure 11. (a) Coercivity distributions of the paleomagnetic endmembers LC (low-coercivity) and HC (high-coercivity) used to reconstruct the natural remanent magnetization demagnetization curves of samples G7 35.7 cm (winter bed) and G7 31.6 cm (summer bed). The endmembers of G7 35.7 cm are represented by Burr Type XII distributions with $\lambda = 15.27$ mT, $\gamma = 1.925$, $\alpha = 0.3901$ (LC), and $\lambda = 135.6$ mT, $\gamma = 2.963$, $\alpha = 3.307$ (HC). The endmembers of G7 31.6 cm are represented by Burr Type XII distributions with $\lambda = 15.13 \times 10^4$ mT, $\gamma = 1.290$, $\alpha = 2{,}047$ (LC), and $\lambda = 116.0$ mT, $\gamma = 2.642$, $\alpha = 1.793$ (HC). (b) Zijderveld plots of samples G7 35.7 cm and G7 31.6 cm with measurements (dots and circles) and the two-endmember model (gray line). The LC and HC endmember directions are indicated by straight dashed lines.

Burr Type XII model functions (Zhao et al., 2016) enables fitting the NRM demagnetization data with Equation 1. The directions of the two endmembers are poorly constrained, due to their sensitivity to the chosen model function and the multiplicity of solutions. Possible solutions for the samples shown in Figure 5 include endmembers with almost antiparallel directions, however, these are associated with unrealistic coercivity distributions (e.g., excessively narrow, with sharp lower/upper limits, or extending to excessively large coercivities). Realistic solutions that minimize the model residuals (Equation 2) and the MADs are shown in Figure 11 for a summer and a winter bed example. The directions of the modeled low- and high-coercivity endmembers are close to the vector differences between the first and last demagnetization steps, respectively, with similar angular differences in both cases. The corresponding coercivity distributions are characterized by median destructive fields of 31–35 and 83–87 mT, respectively, with corresponding dispersion parameters of 0.43–0.60 and 0.21–0.25.

A downcore analysis of the above identified NRM endmembers was performed by identifying the directions of LC and HC with the linear trends of the first (LC) and last (HC) 3 to 5 demagnetization steps in all cases where the directional scatter of these segments did not exceed 5°. LC and HC inclinations are similar for all G7 samples located below ~30 cm (Figures 12a and 12b), while large differences of up to ~22° develop toward the top of the core, with the HC endmember becoming significantly shallower than LC. A large directional scatter is observed between consecutive winter beds, regardless of core depth, while the scatter of summer beds is limited to the upper ~30 cm. Despite this scatter, the inclination difference between the two endmembers defines a continuous trend with no systematic differences between summer and winter beds, going from $\Delta I \approx 0$ at the core bottom, to $\Delta I \approx 20°$ toward the top (Figure 12c). The lack of scatter and systematic seasonal contrasts within this trend suggests that the difference between LC and HC inclinations is governed by extrinsic factors, rather than seasonal changes in sediment composition and short-term disturbances affecting absolute inclination values. Declination differences between LC and HC (Figure 12d) show a similar trend, with no systematic differences between winter and summer beds, albeit more scattered than inclination.

5. Discussion

The aim of this study was to constrain NRM acquisition mechanisms. Several parameters have an impact on magnetic particle alignment by the geomagnetic field (Anson & Kodama, 1987; Arason & Levi, 1990; Katari

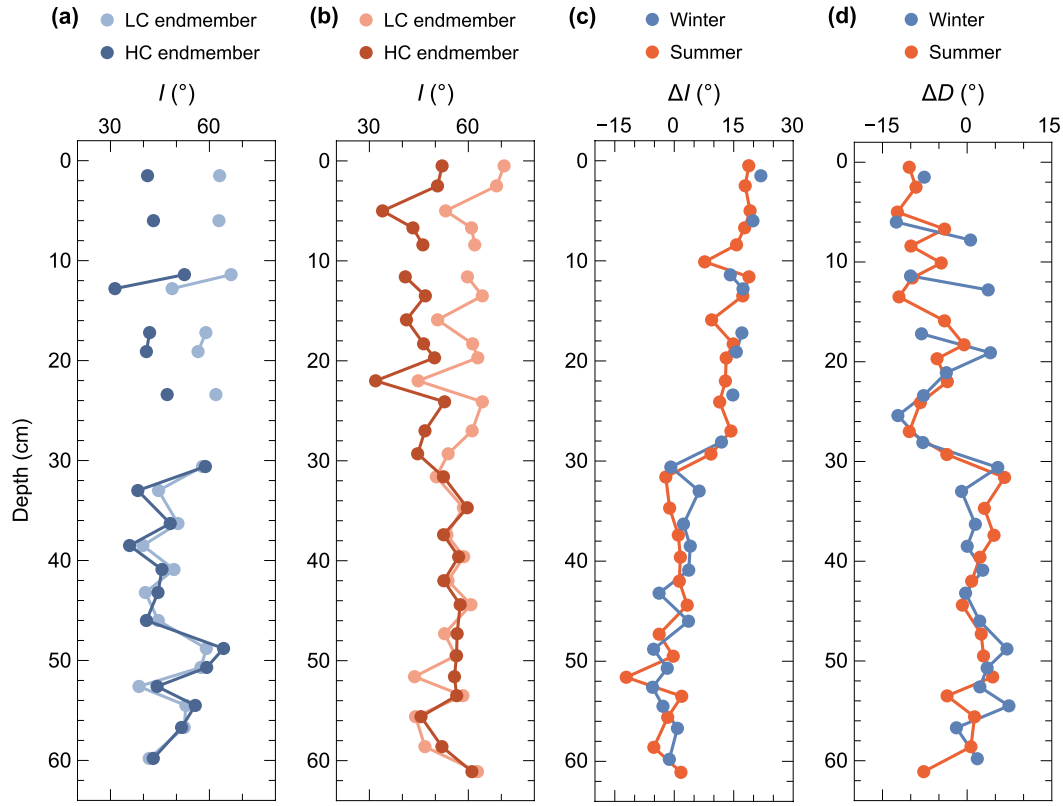

Figure 12. (a) Low-coercivity (LC) and high-coercivity (HC) endmember inclinations in winter beds (dots). Connected dots indicate consecutive beds. (b) Same as (a) for summer beds. (c) Difference between LC and HC inclinations in summer and winter beds. (d) Difference between LC and HC declinations in summer and winter beds.

& Bloxham, 2001; Philippe et al., 2022; Roberts et al., 2013; Shcherbakov & Sycheva, 2010; Tanty et al., 2016; Tauxe, 1993; Tauxe et al., 2006). First, magnetic particle alignment depends on various factors related to depositional conditions and sediment lithology. Varve formation involves reduced turbidity caused by surface ice-cover that allows clay flocculation in winter beds, and increased silt influx in summer (e.g., Smith & Ashley, 1985). Rapidly deposited sediments such as turbidites can record shallow inclinations, with the event size, measured by thickness, determining the extent of the shallowing effect (Philippe et al., 2022; Tanty et al., 2016). Unusually large lock-in depths of up to 30–70 cm, have been reported for varved lake sediments (Mellström et al., 2015; Nilsson et al., 2018), despite the absence of obvious post-depositional sediment mixing. The absence of bioturbation in Lake Ojibway sediments is deduced from varve preservation and the absence of bioturbation traces in the photographs, CT scans and thin-section photographs. The origin of this post-depositional remanent magnetization (PDRM) in varved sediments is unclear and might be related to the formation or chemical transformation of magnetic minerals, leading to the formation of chemical remanent magnetization (CRM), or to compaction-related processes. The major role played by sediment composition and diagenetic processes is underlined in this study by the large differences between the magnetic carriers and the NRM of summer and winter beds.

A notable feature of the Lake Ojibway sediments is the large inclination shallowing of 24.3° ± 8.3° for winter beds and 11.3° ± 7.3° for summer beds, relative to the geomagnetic field at the same latitude and the same epoch (Barletta et al., 2010; Stockhausen, 1998). This creates a ∼13° inclination shallowing differential between the winter and summer beds. The short time span of the studied varve sequence (<7 years; Figure 7) excludes significant paleosecular variations that could explain the recorded values. Winter and summer beds are also characterized by highly contrasting NRM/ARM ratios, with summer figures being, on average, ∼10 times larger than winter ones (Figure 7). For comparison, DRM/ARM values of redeposited single-crystal silicates with magnetic inclusions, which might be associated with the PSD component of Lake Ojibway sediments, differ by up to ∼40% depending on their size and origin (Chang et al., 2021). The mean inclination flattening degree f (King, 1955) of these materials is comprised of 0.3 and 0.4, which, for the site-specific GAD inclination of 67.2°, translates into

an inclination shallowing of 24°–32°. This is compatible with our observations on the inclination; however, the large differences between summer and winter NRM/ARM values cannot be explained by seasonal variations of the detrital input. The interplay between variable detrital and authigenic NRM carriers can also not explain these differences, since the NRM/ARM ratio of detrital and magnetofossil components in pelagic marine sediments has been found to differ by a factor ≤2 (L. Chen et al., 2017).

We are thus left with physical processes affecting NRM acquisition during and after deposition. The NRM acquired by particles settling across shear flows, such as those produced by horizontal currents near the sediment-water interface, is affected by flow characteristics in a complex manner. For instance, Griffiths et al. (1960) reported an increase in the inclination error with increasing flow velocities with an azimuth of 45° with respect to the magnetic field. Significant bottom water circulation during the summer melt could have contributed to reduced summer inclination shallowing compared to the hydrodynamically unperturbed wintertime, as suggested by Griffiths et al. (1960). Griffiths et al. (1960) did not systematically explore the effect of shear flows at different angles to the magnetic field; therefore, these observations cannot be fully related to paleocurrent indicators obtained for instance from magnetic anisotropy. The effect of shear flow on DRM inclination is also demonstrated by speleothems, with >5° shallowing occurring on steep flanks (Ponte et al., 2017).

Rapid deposition events might combine an initial inclination shallowing of DRM with additional compaction effects. According to Tanty et al. (2016), a 47-cm thick turbidite can generate a 13° inclination shallowing. However, the average thickness of summer and winter beds in the G7 sequence (Figure 7) are only 1.76 ± 0.21 and 0.9 ± 0.1 cm, respectively. Compaction can induce substantial inclination shallowing (Anson & Kodama, 1987; Arason & Levi, 1990; Borradaile & Almqvist, 2008; Jackson et al., 1991; Kodama & Sun, 1992). Some experiments indicate a significant effect of compaction on NRM intensity, but not on inclination (e.g., Hamano, 1980). The higher magnetic anisotropy combined with the presence of load structures (i.e., load casts) in the finer-grained winter beds indicates greater compaction compared to the coarser summer beds (Sun & Kodama, 1992). CT number variations (Figure 7) reflect differences in sediment density (e.g., Boespflug et al., 1995; St-Onge et al., 2007). The lower density and higher compressibility of winter beds could be explained by flocculation and higher water contents (e.g., Locat & Lefebvre, 1981; O'Brien & Pietraszek-Mattner, 1998; Quigley et al., 1985).

The ∼24° inclination shallowing of winter beds would require a >50% volume loss in the uppermost few cm of the sediment column (Arason & Levi, 1990). Varved sediments are indeed subjected to a significant amount of compaction, with varve thickness decreasing by up to a factor of 5 during the first few years, followed by a more gradual porosity decrease at greater depths (Maier et al., 2013). Compaction of varved sediment has been clearly linked to the loss of water, as well as an increase in dry sediment density due to organic matter degradation. Under these conditions, the alteration of the sediment microstructure is expected to produce an irreversible rotation of magnetic particles within the sediment matrix, under the action of a magnetic torque induced by the Earth's magnetic field, similar to the case of bioturbated sediment (Egli & Zhao, 2015; Zhao et al., 2016). This process progressively replaces the original DRM with a PDRM that becomes locked at a depth where the torque required to rotate magnetic particles largely exceeds the magnetic torque. Compaction below the lock-in depth produces a further randomization of particle orientation, decreasing the existing NRM intensity without acquiring new magnetization. In the absence of bioturbation, the PDRM acquired in compacting sediment is much smaller than the initial DRM. For instance, a 2-fold decrease in the pore space has been found to produce a four-fold decrease in the PDRM acquisition efficiency (Hamano, 1980). Thus, compaction appears to be the main mechanism responsible for the observed NRM differences between winter and summer beds. The role of compaction is greatly attenuated by bioturbation (Zhao et al., 2016), explaining the lack of extreme downcore variations of the NRM acquisition efficiency and inclination shallowing in most marine sediments.

Fe/κ ratios >40 in the winter beds (49.06 ± 2.05 Mcps) compared to 10.77 ± 1.83 Mcps in the summer bed may suggest a diagenetic influence on NRM acquisition (Hofmann et al., 2005; Hofmann & Fabian, 2009). This hypothesis is also supported by a seasonally oscillating fraction of SD minerals, likely of authigenic origin. The minimum contribution of SD magnetite to the saturation remanence, as deduced from the central ridge in FORC diagrams, reaches ∼10% in winter. Summer beds may contain a minor greigite contribution, which is difficult to quantify. The relative contribution of a CRM to the total NRM is likely much larger, because SD particles carry a saturated natural magnetic moment, compared to the much smaller natural moment of PSD detrital minerals (Chang et al., 2021). Organic matter facilitates sulfate reduction and can generate CRM via greigite formation (Roberts et al., 2011; Thompson & Oldfield, 1986). The low organic matter content of the

studied sediment (<0.25% on average) does not support strong diagenetic processes that lead to a complete chemical remagnetization. While greigite is clearly diagenetic, the origin of SD magnetite particles not associated with magnetofossils, which have been identified in winter beds, is unclear. The pedogenic-like SD component contributing to the central ridge in FORC diagrams of the winter beds (Figure 9b) might represent an authigenic component, but an origin related soil erosion in the catchment area cannot be excluded.

Curved Zijderveld plots (Figure 5) point to a progressive NRM acquisition process that lasts long enough for significant changes of the physical/chemical properties of the sediment and/or the magnetic field direction to occur before the magnetization is completely blocked. Here, we discuss two limit scenarios. In the first case, we assume that the curvature of Zijderveld plots is entirely due to compaction during PDRM acquisition in a fixed magnetic field. This model requires that the HC paleomagnetic endmember (Figure 11) represents a DRM or a PDRM acquired at an early compaction stage, and the LC endmember represents a PDRM acquired at a later stage, when the sediment is already partially compacted. The greater extent of compaction experienced by the HC endmember would cause a stronger inclination shallowing, as indeed observed. The lack of an obvious mechanism capable of making compaction-driven PDRM acquisition depends systematically on the coercivity of magnetic particles represents a main problem for this model. Furthermore, the disappearance of systematic differences between the inclinations of summer and winter beds below ~30 cm (Figure 12) is not related to any obvious change in sediment properties and can therefore not be attributed to the compaction process. Similar reasoning applies to the difference between LC and HC declinations (Figure 12d) because the declination is not expected to be systematically affected by sediment-specific post-depositional processes.

This brings us to the second model for the curvature of Zijderveld plots, where it is assumed that the directional difference between the paleomagnetic endmembers LC and HC is caused by a change in the Earth's magnetic field during the delayed lock-in of one endmember with respect to the other. For instance, LC could be a CRM acquired by SD remanence carriers formed much later after deposition. This scenario is supported by the coercivity distributions of the two endmembers, which roughly match those of the SD and PSD components detected with FORC measurements (Figure 9). In this case, temporal variations $I_{LC}(t - t_{LC})$ and $I_{HC}(t - t_{HC})$ of the LC and HC inclinations, corrected for the corresponding lock-in times t_{LC} and t_{HC}, are expected to yield synchronous reproductions of the field inclination $I_F(t)$, after correcting the inclination shallowing. Inclination shallowing is mathematically described by $\tan I = f \tan I_F$, with $0 < f \leq 1$ (King, 1955; Tauxe & Kent, 1984). Assuming t_0 to be the (uncertain) age of the topmost summer bed in Figure 2, we obtain the following identity

$$\arctan\left[f_{HC}^{-1} \tan I_{HC}(t - t_0)\right] = \arctan\left[f_{LC}^{-1} \tan I_{LC}(t - t_0 - \Delta t)\right] = I_F(t), \quad (3)$$

where f_{HC} and f_{LC} are the flattening factors of the HC and LC endmembers, respectively, Δt the lock-in delay of LC with respect to HC, and I_F the reconstructed local field inclination, for example, from the high-resolution Holocene paleointensity stack for eastern Canada by Barletta et al. (2010). In principle, Equation 3 can be solved for the unknown parameters t_0, Δt, f_{HC}, and f_{LC} by minimizing the RMS difference r_I between I_F and the corrected HC and LC inclinations. A unique solution exists in the case of records that are sufficiently long to capture distinctive field variations.

Shorter records unavoidably yield multiple solutions corresponding to local minima of r_I. In this study, the smallest local minima of r_I are comprised between $t_0 \approx 8.2$ and 8.5 ka, in good agreement with the estimated sediment age (Figure 13a). These minima define a range possible Δt values comprised between −230 a (i.e., the LC endmember is 230 years younger than the HC member), and +240 a (i.e., the LC endmember is 240 years older than the HC member). Two examples corresponding to the smallest minima (Figures 13b and 13c) show that the time interval of ~28 years covered by our record is significantly shorter than the delay between LC and HC acquisition. The solution parameters are entirely determined by the increasing and decreasing trends of $I_{HC}(t)$ and $I_{LC}(t)$, respectively, and not by the large scatter between consecutive values, which, as discussed above, reflects syn- and post-depositional disturbances of the NRM acquisition process, rather than true field variations. Both solutions examples, as well as solutions corresponding to other minima in Figure 13a, are characterized by similar flattening parameters, with $f_{HC} \approx 0.37$ and $f_{LC} \approx 0.49$. For comparison, typical flattening factors reported in the literature are comprised between 0.3 and 1.

If LC and HC are interpreted as endmembers carried by authigenic and detrital minerals, respectively, only the second solution example, where LC is ~182 years younger than HC (Figure 13c), is physically meaningful. In this case, the smaller flattening factor of the LC endmember would be compatible with a PDRM acquired at a later

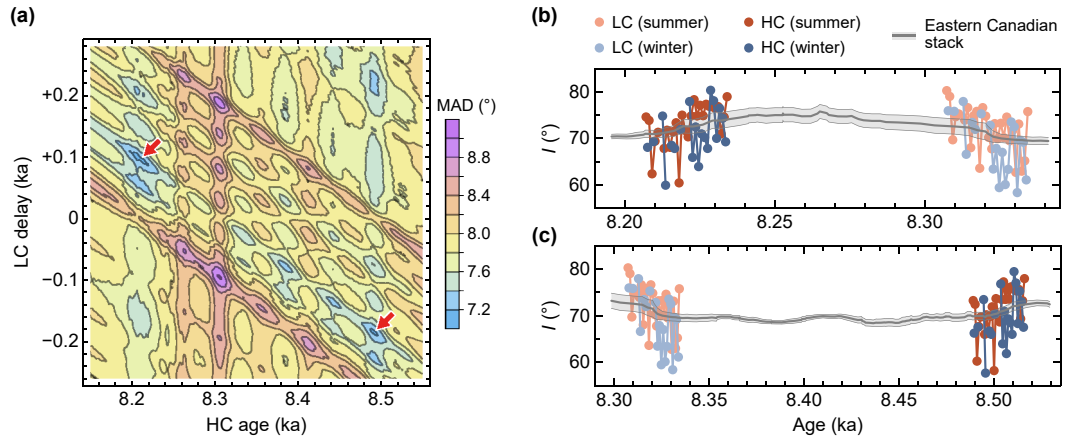

Figure 13. (a) RMS differences between the inclination I_F from the high-resolution Holocene paleointensity stack for eastern Canada (Barletta et al., 2010) and the low-coercivity (LC) and high-coercivity (HC) inclination values of Figure 12, after optimized inclination shallowing correction, as a function of t_0 and Δt. (b) Solution example for $t_0 = 8{,}207.1$ a, $\Delta t = 100.2$ a, $f_{HC} = 0.352$, and $f_{LC} = 0.439$, corresponding to the left arrow in (a). (c) Solution example for $t_0 = 8{,}489.0$ a, $\Delta t = -181.7$ a, $f_{HC} = 0.386$, and $f_{LC} = 0.491$, corresponding to the right arrow in (a).

stage in partially compacted sediment. Given the exceptionally large mean deposition rate of $v_s \approx 20$ mm a^{-1}, the lock-in delay of LC in the example of Figure 13c would yield a lock-in depth of ~3.7 m. Interestingly, this result is compatible with previous paleomagnetic studies based on varved sediments if the lock-in delay, instead of the lock-in depth, is considered: for instance, Δt estimates for the Swedish lakes Gyltigesjön ($v_s = 1.8$ mm a^{-1}) and lake Kälksjön ($v_s = 0.61$ mm a^{-1}) obtained from lock-in depths correspond to 140–200 and 200–300 years, respectively (Nilsson et al., 2018). On the other hand, CRM acquired at several meters' depth by authigenic particles that are nearly equidimensional—as suggested by the coercivity distribution associated with the central ridge, especially in the winter beds—would not be strongly affected by inclination shallowing, because CRM blocking occurs after initial sediment compaction.

The $f_{LC} \approx 0.49$ estimate for the LC endmember thus points to solutions with smaller Δt, even if r_I associated with these solutions is slightly larger than the two solution examples in Figure 13. For instance, the solution corresponding to $t_0 = 8.33$ ka and $\Delta t = -20$ years in Figure 13a yields a lock-in depth of ~40 cm, which is of the same order of magnitude of the solutions reported by Nilsson et al. (2018). Smoothing of the stacked record used as I_F reference could explain the more elevated r_I associated with small-Δt solutions because the rapid inclination changes required by the diverging inclination trends of our endmembers would be partially suppressed.

In the context of this second NRM acquisition model, sediments from Lake Ojibway might reflect a unique setting where the NRM acquired by detrital magnetic minerals during depositions or an early compaction stage is not masked by a strong CRM component, due to limited organic matter availability. The sum of this NRM and a CRM acquired by authigenic SD particles yields curved Zijderveld plots whenever measurable changes of the magnetic field direction occur within the formation time of the authigenic component. Curved Zijderveld plots in marine sediments have been reported in at least one case during the Matuyama-Brunhes field reversal (Valet et al., 2016), and might be explained by a similar mechanism.

6. Conclusions

Analyses of varves from former glacial Lake Ojibway provide information about the NRM acquisition mechanism of unbioturbated sediment deposited in a large and natural depositional basin. The preservation of centimeter-thick varves allows investigation of the magnetic properties of winter and summer beds separately with small 1 cm^3 samples. The dominant characteristic of these varves is the strong contrast between winter and summer paleointensities, and the inclination shallowing of winter beds by ~13° compared to summer beds. We interpret the shallow winter bed inclinations to have been caused by the combined effects of differential compaction generated by the overlying denser summer beds and sediment physical properties (grain size, flocculation). These processes were likely initiated by the large water content of the winter beds. Limited organic matter availability prevented

the formation of large number of diagenetic remanence carriers, leading to the superposition of two paleomagnetic endmembers with overlapping coercivity distributions corresponding to the DRM or PDRM acquired by detrital minerals during or shortly after deposition, and a CRM carried by authigenic magnetite and greigite. The delayed CRM blocking produces curved Zijderveld plots with slightly different endmember directions that are compatible with the location and estimated sediment age.

Seasonal variations of relative paleointensity by a factor of ∼10, as expressed by NRM/ARM in summer and winter beds, cannot be explained only by different remanence carrier compositions, thus demonstrating the utmost importance of syn- and post-depositional processes related to flocculation, deposition, and compaction of sediments in the absence of bioturbation. Variations in the NRM acquisition efficiency by these processes cannot be corrected by normalization procedures used to calculate relative paleointensity. In less extreme cases than the Lake Ojibway example discussed here, this can lead to undetectable recording artifacts, especially in the case of unbioturbated or partially bioturbated sediments.

Data Availability Statement

Data are available at https://doi.pangaea.de/10.1594/PANGAEA.913372.

Acknowledgments
This research was funded by the Natural Sciences and Engineering Research Council of Canada (NSERC) Discovery grants to GSO and PF. We thank Fatoumata Camara at IPGP for her help with sampling and measurement, Laure Meynadier and France Lagroix at IPGP for advice, Geotop for financial support through a scholarship to the first author and Laurie Brown, Andrew P. Roberts and two anonymous reviewers for reviews that improved the manuscript considerably.

References

Amor, M., Wan, J., Egli, R., Carlut, J., Gatel, C., Andersen, I. M., et al. (2022). Key signatures of magnetofossils elucidated by mutant magnetotactic bacteria and micromagnetic calculations. *Journal of Geophysical Research*, *127*(1), e2021JB023239. https://doi.org/10.1029/2021JB023239

Anson, G. L., & Kodama, K. P. (1987). Compaction-induced inclination shallowing of the post-depositional remanent magnetization in a synthetic sediment. *Geophysical Journal International*, *88*(3), 673–692. https://doi.org/10.1111/j.1365-246X.1987.tb01651.x

Antevs, E. (1925). Retreat of the last ice-sheet from eastern Canada. *The Journal of Geology*, *34*, 188.

Arason, P., & Levi, S. (1990). Compaction and inclination shallowing in deep-sea sediments from the Pacific Ocean. *Journal of Geophysical Research*, *95*(B4), 4501–4510. https://doi.org/10.1029/JB095iB04p04501

Barletta, F., St-Onge, G., Stoner, J. S., Lajeunesse, P., & Locat, J. (2010). A high-resolution Holocene paleomagnetic secular variation and relative paleointensity stack from eastern Canada. *Earth and Planetary Science Letters*, *298*(1–2), 162–174. https://doi.org/10.1016/j.epsl.2010.07.038

Bloemendal, J., King, J. W., Hall, F. R., & Doh, S.-J. (1992). Rock magnetism of Late Neogene and Pleistocene deep-sea sediments: Relationship to sediment source, diagenetic processes, and sediment lithology. *Journal of Geophysical Research*, *97*(B4), 4361–4375. https://doi.org/10.1029/91jb03068

Boespflug, X., Long, B. F. N., & Occhietti, S. (1995). CAT-scan in marine stratigraphy: A quantitative approach. *Marine Geology*, *122*(4), 281–301. https://doi.org/10.1016/0025-3227(94)00129-9

Borradaile, G. J., & Almqvist, B. S. (2008). Correcting distorted paleosecular variation in late glacial lacustrine clay. *Physics of the Earth and Planetary Interiors*, *166*(1), 30–43. https://doi.org/10.1016/j.pepi.2007.10.005

Breckenridge, A., Lowell, T. V., Stroup, J. S., & Evans, G. (2012). A review and analysis of varve thickness records from glacial Lake Ojibway (Ontario and Quebec, Canada). *Quaternary International*, *260*, 43–54. https://doi.org/10.1016/j.quaint.2011.09.031

Brouard, E., Roy, M., Godbout, P.-M., & Veillette, J. J. (2021). A framework for the timing of the final meltwater outbursts from glacial Lake Agassiz-Ojibway. *Quaternary Science Reviews*, *274*, 107269. https://doi.org/10.1016/j.quascirev.2021.107269

Chang, L., Hong, H., Bai, F., Wang, S., Pei, Z., Paterson, G. A., et al. (2021). Detrital remanent magnetization of single-crystal silicates with magnetic inclusions: Constraints from deposition experiments. *Geophysical Journal International*, *224*(3), 2001–2015. https://doi.org/10.1093/gji/ggaa559

Chen, A. P., Berounsky, V. M., Chan, M. K., Blackford, M. G., Cady, C., Moskowitz, B. M., et al. (2014). Magnetic properties of uncultivated magnetotactic bacteria and their contribution to a stratified estuary iron cycle. *Nature Communications*, *5*(1), 4797. https://doi.org/10.1038/ncomms5797

Chen, L., Heslop, D., Roberts, A. R., Chang, L., Zhao, X., McGregor, H., et al. (2017). Remanence acquisition efficiency in biogenic and detrital magnetite and recording of geomagnetic paleointensity. *Geochemistry, Geophysics, Geosystems*, *18*(4), 1435–1450. https://doi.org/10.1002/2016GC006753

Clarke, G. K., Leverington, D. W., Teller, J. T., & Dyke, A. S. (2004). Paleohydraulics of the last outburst flood from glacial Lake Agassiz and the 8200 BP cold event. *Quaternary Science Reviews*, *23*(3), 389–407. https://doi.org/10.1016/j.quascirev.2003.06.004

Cogné, J. P. (2003). PaleoMac: A Macintosh™ application for treating paleomagnetic data and making plate reconstructions. *Geochemistry, Geophysics, Geosystems*, *4*(1), 1007. https://doi.org/10.1029/2001GC000227/full

Crémer, J.-F., Long, B., Desrosiers, G., Montety, L. D., & Locat, J. (2002). Application de la scanographie à l'étude de la densité des sédiments et à la caractérisation des structures sédimentaires: Exemple des sédiments déposés dans la rivière saguenay (Québec, Canada) après la crue de juillet 1996. *Canadian Geotechnical Journal*, *39*(2), 440–450. https://doi.org/10.1139/t01-101

Croudace, I. W., Rindby, A., & Rothwell, R. G. (2006). ITRAX: Description and evaluation of a new multi-function X-ray core scanner. *Geological Society, London, Special Publications*, *267*(1), 51–63. https://doi.org/10.1144/GSL.SP.2006.267.01.04

Day, R., Fuller, M., & Schmidt, V. A. (1977). Hysteresis properties of titanomagnetites: Grain-size and compositional dependence. *Physics of the Earth and Planetary Interiors*, *13*(4), 260–267. https://doi.org/10.1016/0031-9201(77)90108-x

Dekkers, M. J., Passier, H. F., & Schoonen, A. A. (2000). Magnetic properties of hydrothermally synthesized greigite (Fe_3S_4), II. High- and low-temperature characteristics. *Geophysical Journal International*, *141*(3), 809–819. https://doi.org/10.1046/j.1365-246x.2000.00129.x

Dunlop, D. J. (2002). Theory and application of the Day plot (Mrs/Ms versus Hcr/Hc) 1. Theoretical curves and tests using titanomagnetite data. *Journal of Geophysical Research*, *107*(B3), 2056. https://doi.org/10.1029/2001JB000486/full

Dyke, A. S. (2004). An outline of North American deglaciation with emphasis on central and northern Canada. *Developments in Quaternary Science*, *2*, 373–424. https://doi.org/10.1016/S1571-0866(04)80209-4

Egli, R. (2003). Analysis of the field dependence of remanent magnetization curves. *Journal of Geophysical Research*, *108*(B2), 2081. https://doi.org/10.1029/2002JB002023

Egli, R. (2004). Characterization of individual rock magnetic components by analysis of remanence curves, 1. Unmixing natural sediments. *Studia Geophysica et Geodaetica*, *48*(2), 391–446. https://doi.org/10.1023/B:SGEG.0000020839.45304.6d

Egli, R. (2013). VARIFORC: An optimized protocol for calculating non-regular first-order reversal curve (FORC) diagrams. *Global and Planetary Change*, *110*, 302–320. https://doi.org/10.1016/j.gloplacha.2013.08.003

Egli, R. (2021). Magnetic characterization of geologic materials with first-order reversal curves. *Magnetic measurement techniques for materials characterization*, 455–604. https://doi.org/10.1007/978-3-030-70443-8_17

Egli, R., Chen, A. P., Winklhofer, M., Kodama, K. P., & Horng, C.-S. (2010). Detection of noninteracting single domain particles using first-order reversal curve diagrams. *Geochemistry, Geophysics, Geosystems*, *11*(1), Q01Z11. https://doi.org/10.1029/2009GC002916

Egli, R., & Zhao, X. (2015). Natural remanent magnetization acquisition in bioturbated sediment: General theory and implications for relative paleointensity reconstructions. *Geochemistry, Geophysics, Geosystems*, *16*(4), 995–1016. https://doi.org/10.1002/2014GC005672

Feinberg, J. M., Scott, G. R., Renne, P. R., & Wenk, H.-R. (2005). Exsolved magnetite inclusions in silicates: Features determining their remanence behavior. *Geology*, *33*(6), 513–516. https://doi.org/10.1130/G21290.1

Fortin, D., Francus, P., Gebhardt, A. C., Hahn, A., Kliem, P., Lisé-Pronovost, A., et al. (2013). Destructive and non-destructive density determination: Method comparison and evaluation from the Laguna Potrok Aike sedimentary record. *Quaternary Science Reviews*, *71*, 147–153. https://doi.org/10.1016/j.quascirev.2012.08.024

Francus, P., & Asikainen, C. A. (2001). Sub-sampling unconsolidated sediments: A solution for the preparation of undisturbed thin-sections from clay-rich sediments. *Journal of Paleolimnology*, *26*(3), 323–326. https://doi.org/10.1023/A:1017572602692

Francus, P., Bradley, R. S., Abbott, M. B., Patridge, W., & Keimig, F. (2002). Paleoclimate studies of minerogenic sediments using annually resolved textural parameters. *Geophysical Research Letters*, *29*(20), 1998–59-4. https://doi.org/10.1029/2002GL015082

Godbout, P.-M., Roy, M., & Veillette, J. J. (2019). High-resolution varve sequences record one major late-glacial ice readvance and two drainage events in the eastern Lake Agassiz-Ojibway basin. *Quaternary Science Reviews*, *223*, 105942. https://doi.org/10.1016/j.quascirev.2019.105942

Godbout, P.-M., Roy, M., & Veillette, J. J. (2020). A detailed lake-level reconstruction shows evidence for two abrupt lake drawdowns in the late-stage history of the eastern Lake Agassiz-Ojibway basin. *Quaternary Science Reviews*, *238*, 106327. https://doi.org/10.1016/j.quascirev.2020.106327

Griffiths, D. H., King, R. F., Rees, A. I., & Wright, A. E. (1960). The remanent magnetism of some recent varved sediments. *Proceedings of the Royal Society of London. Series A. Mathematical and Physical Sciences*, *256*(1286), 359–383. Retrieved from http://rspa.royalsocietypublishing.org/content/256/1286/359.short

Hamano, Y. (1980). An experiment on the post-depositional remanent magnetization in artificial and natural sediments. *Earth and Planetary Science Letters*, *51*(1), 221–232. https://doi.org/10.1016/0012-821X(80)90270-8

Hofmann, D. I., & Fabian, K. (2009). Correcting relative paleointensity records for variations in sediment composition: Results from a South Atlantic stratigraphic network. *Earth and Planetary Science Letters*, *284*(1), 34–43. https://doi.org/10.1016/j.epsl.2009.03.043

Hofmann, D. I., Fabian, K., Schmieder, F., Donner, B., & Bleil, U. (2005). A stratigraphic network across the Subtropical Front in the central South Atlantic: Multi-parameter correlation of magnetic susceptibility, density, X-ray fluorescence and $\delta^{18}O$ records. *Earth and Planetary Science Letters*, *240*(3), 694–709. https://doi.org/10.1016/j.epsl.2005.09.048

Jackson, M. J., Banerjee, S. K., Marvin, J. A., Lu, R., & Gruber, W. (1991). Detrital remanence, inclination errors, and anhysteretic remanence anisotropy: Quantitative model and experimental results. *Geophysical Journal International*, *104*(1), 95–103. https://doi.org/10.1111/j.1365-246X.1991.tb02496.x

Jelinek, V. (1981). Characterization of the magnetic fabric of rocks. *Tectonophysics*, *79*(3), T63–T67. https://doi.org/10.1016/0040-1951(81)90110-4

Katari, K., & Bloxham, J. (2001). Effects of sediment aggregate size on DRM intensity: A new theory. *Earth and Planetary Science Letters*, *186*(1), 113–122. https://doi.org/10.1016/s0012-821x(00)00386-1

Katari, K., Tauxe, L., & King, J. (2000). A reassessment of post-depositional remanent magnetism: Preliminary experiments with natural sediments. *Earth and Planetary Science Letters*, *183*(1), 147–160. https://doi.org/10.1016/s0012-821x(00)00255-7

King, R. F. (1955). The remanent magnetism of artificially deposited sediments. *Geophysical Journal International*, *7*, 115–134. https://doi.org/10.1111/j.1365-246x.1955.tb06558.x

Kodama, K. P., & Sun, W. W. (1992). Magnetic anisotropy as a correction for compaction-caused palaeomagnetic inclination shallowing. *Geophysical Journal International*, *111*(3), 465–469. https://doi.org/10.1111/j.1365-246X.1992.tb02104.x

Lajeunesse, P., & St-Onge, G. (2008). The subglacial origin of the Lake Agassiz-Ojibway final outburst flood. *Nature Geoscience*, *1*(3), 184–188. https://doi.org/10.1038/ngeo130

Lanci, L., & Kent, D. V. (2018). Forward modeling of thermally activated single-domain magnetic particles applied to first-order reversal curves. *Journal of Geophysical Research: Solid Earth*, *123*(5), 3287–3300. https://doi.org/10.1002/2018JB015463

Lascu, I., Ensle, J. F., Ball, M. R., & Harrison, R. J. (2018). The vortex state in geologic materials: A micromagnetic perspective. *Journal of Geophysical Research: Solid Earth*, *123*(9), 7285–7304. https://doi.org/10.1029/2018JB015909

Locat, J., & Lefebvre, G. (1981). Étude de la formation des sédiments fins glacio-lacustres du lac Barlow-Ojibway: Le site d'Olga, Matagami, Québec. *Géographie Physique et Quaternaire*, *35*(1), 93–103. https://doi.org/10.7202/1000381ar

Maier, D. B., Rydberg, J., Bigler, C., & Renberg, I. (2013). Compaction of recent varved lake sediments. *GFF*, *135*(3–4), 231–236. https://doi.org/10.1080/11035897.2013.788551

Mellström, A., Nilsson, A., Stanton, T., Muscheler, R., Snowball, I., & Suttie, N. (2015). Post-depositional remanent magnetization lock-in depth in precisely dated varved sediments assessed by archaeomagnetic field models. *Earth and Planetary Science Letters*, *410*, 186–196. https://doi.org/10.1016/j.epsl.2014.11.016

Moskowitz, B. M. (1991). Hitchhiker's guide to magnetism. In *Environmental magnetism workshop (IRM)* (Vol. 279, p. 48).

Moskowitz, B. M., Frankel, R. B., & Bazylinski, D. A. (1993). Rock magnetic criteria for the detection of biogenic magnetite. *Earth and Planetary Science Letters*, *120*(3–4), 283–300. https://doi.org/10.1016/0012-821X(93)90245-5

Nagata, T. (1961). *Rock magnetism* (p. 350). Maruzen.

Nagy, L., Williams, W., Tauxe, L., & Muxworthy, A. R. (2019). From nano to micro: Evolution of magnetic domain structures in multidomain magnetite. *Geochemisty, Geophysics, Geosystems*, *20*(6), 2907–2918. https://doi.org/10.1029/2019GC008319

Nilsson, A., Suttie, N., & Hill, M. J. (2018). Short-term magnetic field variations from the post-depositional remanence of Lake sediments. *Frontiers of Earth Science*, *6*, 39. https://doi.org/10.3389/feart.2018.00039

O'Brien, N. R., & Pietraszek-Mattner, S. (1998). Origin of the fabric of laminated fine-grained glaciolacustrine deposits. *Journal of Sedimentary Research*, *68*(5), 832–840. https://doi.org/10.2110/jsr.68.832

Philippe, É. G. H., Valet, J.-P., St-Onge, G., & Egli, R. (2022). Impact of turbulence on magnetic alignment in sediments. *Frontiers of Earth Science*, *10*, 1079229. https://doi.org/10.3389/feart.2022.1079229

Philippe, É. G. H., Valet, J.-P., St-Onge, G., & Thevarasan, A. (2018). Are paleomagnetic records from U-channels Appropriate for studies of reversals and excursions? *Geochemistry, Geophysics, Geosystems*, *19*(11), 4130–4142. https://doi.org/10.1029/2018GC007803

Ponte, J. M., Font, E., Velga-Pires, C., Hillaire-Marcel, C., & Ghaleb, B. (2017). The effect of speleothem surface slope on the remanent magnetic inclination. *Journal of Geophysical Research: Solid Earth*, *122*(6), 4143–4156. https://doi.org/10.1002/2016JB013789

Quigley, R. M., Sethi, A. J., Boonsinsuk, P., Sheeran, D. E., & Yong, R. N. (1985). Geologic control on soil composition and properties, Lake Ojibway clay plain, Matagami, Quebec. *Canadian Geotechnical Journal*, *22*(4), 491–500. https://doi.org/10.1139/t85-069

Ridge, J. C., Brennan, W. J., & Muller, E. H. (1990). The use of paleomagnetic declination to test correlations of late Wisconsinan glaciolacustrine sediments in central New York. *GSA Bulletin*, *102*(1), 26–44. https://doi.org/10.1130/0016-7606(1990)102<0026:TUOPDT>2.3.CO;2

Roberts, A. P., Almeida, T. P., Church, N. S., Harrison, R. J., Heslop, D., Li, Y., et al. (2017). Resolving the origin of pseudo-single domain magnetic behavior. *Journal of Geophysical Research: Solid Earth*, *122*(12), 9534–9558. https://doi.org/10.1002/2017JB014860

Roberts, A. P., Chang, L., Rowan, C. J., Horng, C.-S., & Florindo, F. (2011). Magnetic properties of sedimentary greigite (Fe_3S_4): An update. *Reviews of Geophysics*, *49*(1), RG1002. https://doi.org/10.1029/2010RG000336

Roberts, A. P., Tauxe, L., & Heslop, D. (2013). Magnetic paleointensity stratigraphy and high-resolution quaternary geochronology: Successes and future challenges. *Quaternary Science Reviews*, *61*, 1–16. https://doi.org/10.1016/j.quascirev.2012.10.036

Rothwell, R. G., Hoogakker, B., Thomson, J., Croudace, I. W., & Frenz, M. (2006). Turbidite emplacement on the southern Balearic Abyssal plain (western Mediterranean sea) during marine isotope stages 1–3: An application of ITRAX XRF scanning of sediment cores to lithostratigraphic analysis. *Geological Society, London, Special Publications*, *267*(1), 79–98. https://doi.org/10.1144/GSL.SP.2006.267.01.06

Rowan, C. J., & Roberts, A. P. (2006). Magnetite dissolution, diachronous greigite formation, and secondary magnetizations from pyrite oxidation: Unravelling complex magnetizations in Neogene marine sediments from New Zealand. *Earth and Planetary Science Letters*, *241*(1–2), 119–137. https://doi.org/10.1016/j.epsl.2005.10.017

Roy, M., Dell'Oste, F., Veillette, J. J., de Vernal, A., Hélie, J.-F., & Parent, M. (2011). Insights on the events surrounding the final drainage of Lake Ojibway based on James Bay stratigraphic sequences. *Quaternary Science Reviews*, *30*(5), 682–692. https://doi.org/10.1016/j.quascirev.2010.12.008

Roy, M., Veillette, J. J., Daubois, V., & Ménard, M. (2015). Late-stage phases of glacial Lake Ojibway in the central Abitibi region, eastern Canada. *Geomorphology*, *248*, 14–23. https://doi.org/10.1016/j.geomorph.2015.07.026

Shcherbakov, V., & Sycheva, N. (2010). On the mechanism of formation of depositional remanent magnetization. *Geochemistry, Geophysics, Geosystems*, *11*(2), Q07Y10. https://doi.org/10.1029/2009GC002830/full

Smith, N. D., & Ashley, G. (1985). Proglacial lacustrine environment. In *Society of economic paleontologists and mineralogists, short course* (Vol. 16, pp. 135–216).

Spassov, S., & Valet, J.-P. (2012). Detrital magnetizations from redeposition experiments of different natural sediments. *Earth and Planetary Science Letters*, *351*, 147–157. https://doi.org/10.1016/j.epsl.2012.07.016

Stockhausen, H. (1998). Geomagnetic palaeosecular variation (0–13 000 yr BP) as recorded in sediments from three maar lakes from the West Eifel (Germany). *Geophysical Journal International*, *135*(3), 898–910. https://doi.org/10.1046/j.1365-246X.1998.00664.x

Stoner, J. S., & St-Onge, G. (2007). Chapter three magnetic stratigraphy in paleoceanography: Reversals, excursions, paleointensity, and secular variation. *Developments in Marine Geology*, *1*, 99–138. https://doi.org/10.1016/S1572-5480(07)01008-1

St-Onge, G., Mulder, T., Francus, P., & Long, B. (2007). Chapter two continuous physical properties of cored marine sediments. *Developments in marine geology*, *1*, 63–98. https://doi.org/10.1016/S1572-5480(07)01007-X

Striberger, J., Björck, S., Ingólfsson, Ó., Kjær, K. H., Snowball, I., & Uvo, C. B. (2011). Climate variability and glacial processes in eastern Iceland during the past 700 years based on varved lake sediments. *Boreas*, *40*(1), 28–45. https://doi.org/10.1111/j.1502-3885.2010.00153.x

Stroup, J. S., Lowell, T. V., & Breckenridge, A. (2013). A model for the demise of large, glacial Lake Ojibway, Ontario and Quebec. *Journal of Paleolimnology*, *50*(1), 105–121. https://doi.org/10.1007/s10933-013-9707-9

Sun, W. W., & Kodama, K. P. (1992). Magnetic anisotropy, scanning electron microscopy, and X ray pole figure goniometry study of inclination shallowing in a compacting clay-rich sediment. *Journal of Geophysical Research*, *97*(B13), 19599–19615. https://doi.org/10.1029/92JB01589

Tanty, C., Valet, J.-P., Carlut, J., Bassinot, F., & Zaragosi, S. (2016). Acquisition of detrital magnetization in four turbidites. *Geochemistry, Geophysics, Geosystems*, *17*(8), 3207–3223. https://doi.org/10.1002/2016GC006378

Tauxe, L. (1993). Sedimentary records of relative paleointensity of the geomagnetic field: Theory and practice. *Reviews of Geophysics*, *31*(3), 319–354. https://doi.org/10.1029/93rg01771

Tauxe, L., & Kent, D. V. (1984). Properties of a detrital remanence carried by haematite from study of modern river deposits and laboratory redeposition experiments. *Geophysical Journal of the Royal Astronomical Society*, *77*(3), 543–561. https://doi.org/10.1111/j.1365-246X.1984.tb01909.x

Tauxe, L., Steindorf, J. L., & Harris, A. (2006). Depositional remanent magnetization: Toward an improved theoretical and experimental foundation. *Earth and Planetary Science Letters*, *244*(3), 515–529. https://doi.org/10.1016/j.epsl.2006.02.003

Thébault, E., Finlay, C. C., Beggan, C. D., Alken, P., Aubert, J., Barrois, O., et al. (2015). International geomagnetic reference field: The 12th generation. *Earth Planets and Space*, *67*(1), 79. https://doi.org/10.1186/s40623-015-0228-9

Thompson, R., & Oldfield, F. (1986). *Chapter four environmental magnetism* (Vol. 21–38). Allen and Unwin.

Thorleifson, L. H., Teller, J. T., Matile, G., & Brisbin, W. C. (1996). Review of Lake Agassiz history. Sedimentology, geomorphology, and history of the central Lake Agassiz basin. In *Geological association of Canada field trip guidebook B* (Vol. 2, pp. 55–84).

Till, J. L., Guyodo, Y., Lagroix, F., Morin, G., Menguy, N., & Ona-Nguema, G. (2017). Presumed magnetic biosignatures observed in magnetite derived from abiotic reductive alteration of nanogoethite. *Comptes Rendus Geoscience*, *349*(2), 63–70. https://doi.org/10.1016/j.crte.2017.02.001

Valet, J.-P., Meynadier, L., Simon, Q., & Thouveny, N. (2016). When and why sediments fail to record the geomagnetic field during polarity reversals. *Earth and Planetary Science Letters*, *453*, 96–107. https://doi.org/10.1016/j.epsl.2016.07.055

Valet, J.-P., Tanty, C., & Carlut, J. (2017). Detrital magnetization of laboratory-redeposited sediments. *Geophysical Journal International*, *210*(1), 34–41. https://doi.org/10.1093/gji/ggx139

Veillette, J. J. (1994). Evolution and paleohydrology of glacial lakes Barlow and Ojibway. *Quaternary Science Reviews*, *13*(9), 945–971. https://doi.org/10.1016/0277-3791(94)90010-8

Yoshida, S., & Katsura, I. (1985). Characterization of fine magnetic grains in sediments by the suspension method. *Geophysical Journal International*, *82*(2), 301–317. https://doi.org/10.1111/j.1365-246X.1985.tb05139.x

Zhao, X., Egli, R., Gilder, S., Xu, Y., He, K., & Müller, S. (2016). Microbially-assisted recording of the Earth's magnetic field in sediment. *Nature Communications*, *7*(1), 10673. https://doi.org/10.1028/ncomms10673